Salt-magma interactions influence intrusion distribution and salt tectonics in the Santos Basin, offshore Brazil

Running title: Salt-magma interaction

Craig Magee[1]*, Leonardo Muniz-Pichel[2], Amber L. Madden-Nadeau[3], Christopher A-L. Jackson[2], Webster Mohriak[4]

[1]School of Earth and Environment, University of Leeds, Leeds, LS2 9JT, UK

[2]Basins Research Group, Department of Earth and Environment, Imperial College London, London, SW7 2BP, UK

[3]Department of Earth Sciences, University of Oxford, Oxford, OX1 3AN, UK

[4]Faculty of Geology, Universidade do Estado do Rio De Janeiro, Rio de Janeiro, Brazil

Correspondence (c.magee@leeds.ac.uk)

ORCiD: Craig Magee (0000-0001-9836-2365)

ACKNOWLEDGEMENTS

We are grateful to ANP for providing and permitting us to publish the seismic reflection data and to Schlumberger for the interpretation software. We thank Imperial College London UROP scheme for funding AM-N in the initial phase of this work.

DATA AVAILABILITY

The seismic reflection data that support the findings of this study are available from ANP but restrictions apply to the availability of these data, which were used under a confidentiality agreement for the current study, and so are not publicly available.

CONFLICT OF INTEREST

The authors declare there are no conflicts of interest.

ABSTRACT

Many sedimentary basins host thick evaporite (salt) deposits. Some of these basins also host extensive igneous intrusion networks. It thus seems inevitable that, in some locations, magma will interact with salt. Yet how interaction between these materials may influence salt tectonics or magma emplacement, particularly at the basin-scale, remains poorly understood. We use 3D seismic reflection data from the Santos Basin, offshore Brazil to image 38 igneous intrusions spatially related to thick Aptian salt. We show intra-salt sills are geometrically similar to but laterally offset from supra-salt sills. We suggest ascending magma was arrested by the salt in some areas, but not others, perhaps due to differences in evaporite lithology. Our mapping also reveals most sills occur within and above the pre-salt Merluza Graben, an area characterised by Albian-to-Neogene, salt-detached extension. In adjacent areas, where there are few intrusions, salt deformation was driven by post-Santonian diapir rise. We suggest emplacement of hot magma within evaporites above the Merluza Graben enhanced Albian-to-Santonian salt movement, but that crystallisation of the intrusion network restricted post-Santonian diapirism. Our work indicates salt-magma interaction can influence salt tectonics, as well as the distribution of magma plumbing systems, and thus could impact basin evolution.

KEYWORDS: salt, magma, sill, tectonics, basin, Brazil

INTRODUCTION

Thick evaporite deposits are common in many sedimentary basins, where they can flow to form a range of salt structures (e.g., diapirs) [e.g., Hudec and Jackson, 2007; Jackson, 1995; Rowan, 2014; Rowan et al., 2004; Warren, 2006; Warren, 2010]. Many salt basins also contain magma plumbing systems, which in places may have intruded earlier salt-formed structures [North Sea, offshore Netherlands, Blažić and Moreau, 2017; e.g., Danakil Depression, Ethiopia, Schofield et al., 2014]. On their own, both salt tectonics and magmatism can impact the evolution of sedimentary basins and continental margins, including the accumulation of natural resources [e.g., Bedard et al., 2012; Holford et al., 2012; Jackson and Hudec, 2017; Peron-Pinvidic et al., 2019; Rohrman, 2007; Schofield et al., 2017; Skogseid et al., 2000; Tari et al., 2003]. Yet despite the common occurrence of igneous intrusions in many salt basins, and their importance to basin evolution and natural resource development, we have a poor understanding of how magma may interact physically and chemically with salt, or the potential consequences of such interactions [e.g., Heimdal et al., 2019; Li et al., 2009; Schofield et al., 2014].

Few structurally oriented studies have explored potential salt-magma interactions [Schofield et al., 2014; Underhill, 2009]. For example, Schofield et al. [2014] showed mechanical variations within the sub-horizontally layered, Werra salt complex, Germany, locally controlled magma emplacement mechanics and intrusion architecture at a metre-scale. In the Werra salt-complex, relatively strong halite layers were shown to host vertical dykes emplaced via brittle processes, whereas syn-intrusion heating, dehydration, and fluidization of hydrous salt (e.g., carnallite) layers promoted sill emplacement [Schofield et al., 2014]. However, it remains unclear whether and how these salt-magma interactions occur at the basin-scale [Schofield et al., 2014]; for example, can salt bodies provide preferential flow pathways for magma, or do they arrest intrusions and restrict magma distribution? Furthermore, we do not fully know: (i) whether emplacement of hot magma could induce salt flow [Underhill, 2009]; or (ii) if the intrusion and crystallization of magma within hydrous salts like carnallite, which can lubricate and facilitate salt movement [e.g., Jackson and Hudec, 2017; Urai et al., 1986; Van Keken et al., 1993], could inhibit salt flow and thereby limit diapirism [e.g., Schofield et al., 2014]. There is also a lack of information regarding how the heating and potential melting of salt (e.g., halite melts at ~800 °C) during intrusion affects the chemistry, rheology, and evolution of a magma and/or the formation of associated ore deposits [e.g., Barton and Johnson, 1996; Heimdal et al., 2019; Iacono-Marziano et al., 2017; Li et al., 2009; Mohriak et al., 2009; Pang et al., 2013; Ripley et al., 2003].

There are two key problems that currently limit our ability to answer questions regarding salt-magma interactions. First, field or mine exposures of intrusions within salt allow chemical and small-scale (e.g., metre-scale) structural analysis of salt-magma interactions, but provide little insight into how the whole system may have behaved in 3D at substantially larger scales [e.g., Schofield et al., 2014]. Second, seismic reflection images reveal the 3D architecture of entire intrusions, salt structures, and halokinetic sequences, but provide little insight into the chemical or small-scale structural processes associated with salt-magma interaction [cf. Blažić and Moreau, 2017; Underhill, 2009]. Integrating field and seismic datasets will arguably be critical to addressing the shortcomings associated with each data-type.

Here we use 3D seismic reflection data from the Santos Basin, offshore Brazil to image the structure of 38 igneous intrusions emplaced below, within, and above an Aptian evaporite layer that flowed to form a range of kilometre-scale salt structures. No boreholes in the study area penetrate the salt structures or sills, meaning we cannot directly comment on small-scale structural and chemical salt-magma interactions. However, with our data, we aim to establish the basin-scale structural consequences of salt-magma interactions, allowing us to test whether: (i) the behaviour and rheological properties of salt during emplacement can influence the geometry of individual intrusions and intrusion networks; (ii) salt layers can facilitate or inhibit magma ascent; and (iii) the presence of magma or crystallised intrusions impacts large-scale salt tectonics. By evaluating the consequences of magma intrusion within salt, we anticipate our research will provide a framework for future, integrative studies probing physical and chemical salt-magma interactions at a variety of scales.

GEOLOGICAL SETTING

The Santos Basin located offshore south-eastern Brazil and formed in the Early Cretaceous (~130–125 Ma; Barremian-to-Early Aptian) due to the opening of the South Atlantic Ocean (Figs 1a and b) [e.g., Davison et al., 2012; Mohriak et al., 1995; Quirk et al., 2012]. During the post-rift, in the latest Aptian to possibly earliest Albian (~116–111 Ma), a ~2–3.5 km thick evaporite-dominated layer was deposited across the basin, covering a sag basin sedimentary succession (Figs 1a and b) [e.g., Davison et al., 2012; Karner and Gambôa, 2007; Pichel and Jackson, 2020; Rowan, 2014].

Relief across the base salt horizon, a relic of prior rifting (e.g., the Merluza Graben), and at least 12 cycles of basin desiccation and filling controlled initial thickness, compositional, and rheological variations within the salt layer [e.g., Davison et al., 2012; Jackson et al., 2015b; Pichel et al., 2018; Rodriguez et al., 2018]. For example, the salt layer can be divided into four units (A1-A4) based on their distinct composition (using borehole data) and seismic expression elsewhere in the Santos Basin [Rodriguez et al., 2018]. Units A1 and A3 are characterized by low-frequency, transparent and chaotic seismic facies, and represent halite-rich (>85%) units, whereas high-frequency, highly reflective seismic facies (A2 and A4) correspond to halite-rich (~65%–85% halite) layers that contain relatively high proportions (~15%–35%) of anhydrite and bittern salts (i.e., K- and Mg-rich salts) [Rodriguez et al., 2018]. Evaporites in our study area were deposited across a prominent pre-salt rift topography, with base-salt relief of up to ~1 km controlled by ~NE-trending, high-displacement (~0.5–1 km) normal faults associated with the ~150 km long, up to ~4 km deep, pre- to syn-salt Merluza Graben (Fig. 1c) [e.g., Mohriak et al., 2010]. Cessation of evaporite deposition in the early Albian marked the establishment of permanent marine conditions in the Santos Basin and formation of a proximal carbonate platform (Fig. 1b) [e.g., Karner and Gambôa, 2007; Meisling et al., 2001; Modica and Brush, 2004]. Igneous intrusions and extrusions were emplaced after salt deposition, particularly during discrete phases at ~90–80 Ma and ~60–40 Ma, across the Santos and Campos basins [see Oreiro et al., 2008 and references therein].

Salt tectonics across the Santos Basin resulted in the development of kinematically-linked domains of up-dip extension, intermediate translation, and down-dip contraction and salt extrusion (Figs 1b and c) [e.g., Davison et al., 2012; Demercian et al., 1993; Jackson et al., 2015b; Pichel et al., 2018; Rodriguez et al., 2018]. Regional salt deformation in the Santos Basin started during the Albian, immediately following evaporite deposition (Fig. 1b). South-eastwards tilting of the basin as the Brazilian continental margin thermally subsided produced an array of thin-skinned, salt-detached, normal faults that (Fig. 1c): (i) dismembered the Albian succession into extensional rafts and produced salt rollers [cf. Brun and Mauduit, 2009; Vendeville and

Jackson, 1992] in the up-dip proximal domain, where our study area is located; and (ii) instigated down-dip salt inflation and contraction, producing salt anticlines and buckle-folds [e.g., Davison et al., 2012; Demercian et al., 1993; Jackson et al., 2015a; Quirk et al., 2012]. Salt tectonics continued throughout the Late Cretaceous and early Cenozoic as the basin-margin clastic sediments prograded south-eastwards across the salt (Fig. 1c) [Davison et al., 2012; Guerra and Underhill, 2012; Jackson et al., 2015b; Pichel et al., 2019b]. Post-Albian up-dip extension involved continuous development of salt rollers and reactive (i.e. extensional) diapirs, which resulted in the formation of a large (>50 km wide), oceanward-dipping rollover within the Late Cretaceous and early Cenozoic strata (Fig. 1c) [e.g., Jackson et al., 2015b; Mohriak et al., 1995; Pichel and Jackson, 2020]. Intermediate translation during this period was characterised by the development of ramp-syncline basins, passive diapirs, and localized contraction and extension occurring in response to salt movement over a prominent base-salt relief (Fig. 1c) [e.g., Dooley et al., 2020; Pichel et al., 2019b; Pichel et al., 2018]. Down-dip contraction was associated with salt thickening, development of salt-cored folds, thrusts, and squeezed (active) diapirs, as well as the advancement of a salt nappe beyond the south-eastern edge of the salt basin (Fig. 1c) [e.g., Davison et al., 2012; Demercian et al., 1993; Mohriak et al., 2009; Quirk et al., 2012].

DATASET AND METHODS

We use a ~1000 km^2, time-migrated 3D seismic volume, which has a line spacing of 12.5 m and 25 m and a record length of ~9 seconds two-way travel-time (s TWT). The data were acquired in 2006 using 10, 6 km long streamers and a shot interval of 25 m with a sample rate of 2 ms. We present the minimum phase processed data with an SEG (Society of Economic Geologists) normal polarity, whereby a downwards decrease in acoustic impedance corresponds to a positive (red) reflection. We do not have access to any boreholes within the study so cannot constrain seismic velocities for the interval of interest and, therefore, estimate the spatial resolution of the seismic data. Although the absence of resolution information inhibits quantitative analyses of small-scale features (e.g., intrusive steps) and structure dimensions (e.g., sill thickness), it does not impede a comparison between salt structures and igneous intrusions that are typically hundreds of metres to a few kilometres in scale. The lack of well data also means we cannot confidently determine the age or lithology of intra-salt layers (e.g., A1-A4) or supra-salt strata, although we can still establish relative timings from superposition. To provide some stratigraphic context and chronological framework, we approximately constrain the ages of our mapped horizons through visual comparison to those identified in Pequeno [2009], who used data from 24 confidential, but unnamed, boreholes (Fig. 1b).

Horizon mapping

We mapped the top salt (TS), which corresponds to the near Top Aptian and approximate base salt (BS) horizons (Figs 1b and 2). Time-structure maps of BS and TS provide information on the pre-salt basin structure and post-depositional deformation of the salt, respectively. We also mapped eight supra-salt salt horizons to constrain the present geometry of the overburden (Figs 1b and 2). Based on comparison to horizons dated by Pequeno [2009], we mapped (Figs 1b and 2): H1 = near Cenomanian-Turonian boundary; H2 = near Coniacian-Santonian boundary; H3 = near Top Santonian; H4 = intra-Campanian; H5 = near Top Campanian; H6 = near Top Cretaceous; H7 = intra-Paleogene; and H8 = intra-Neogene. Time-thickness (isochore) maps record changes in salt-controlled accommodation between these supra-salt horizons, which allowed us to unravel the salt deformation history. To quantify how stratal thickness varies across some salt-detached faults, we calculated expansion indices; i.e. the ratio of the hanging wall thickness of a sedimentary sequence to its footwall thickness [e.g., Thorsen, 1963]. Expansion indices >1 for a stratigraphic unit indicate the fault was surface breaking during its deposition, with fault slip accommodating additional sediment and an overall thicker succession in its hanging wall, compared to its footwall [e.g., Thorsen, 1963].

We mapped 38 igneous intrusions based on whether their corresponding reflections were high-amplitude, positive-polarity, laterally discontinuous (on a kilometre scale), and/or transgressed background stratigraphic or salt-related reflections [e.g., Planke et al., 2005]. Each intrusion is expressed as a tuned reflection package, whereby seismic energy returned from the top and base contacts convolves as it travels back to the surface and cannot be distinguished (e.g., Fig. 2) [e.g., Brown, 2011]. For the 18 mapped intra-salt sills, it is plausible that their high-amplitude, positive polarity, and discontinuity could be attributed to the presence of relatively dense and/or high-velocity salt lithologies (e.g., anhydrite, carbonate, and carnallite) within encasing halite [e.g., Jackson et al., 2015b; Rodriguez et al., 2018]. However, we observe that, in places, sub-salt and intra-salt reflections cross-cut BS and TS, respectively; the strata-discordant nature of these reflections, which do not offset horizons, supports our interpretation that they correspond to igneous intrusions [e.g., Planke et al., 2005]. We do recognise other high-amplitude, positive-polarity, laterally discontinuous reflections within the salt but did not map these as they display complex, incoherent geometries in 3D, which complicates their characterisation (e.g., Fig. 2); i.e. we could not establish whether these reflections likely corresponded to igneous intrusions or other intra-salt material (e.g., stringers). Furthermore, we acknowledge that thin sills, with thicknesses below the limit of visibility of the data, may not be recognised within the data [e.g., Eide et al., 2018; Schofield et al., 2017]. No dykes were identified in the seismic reflection data, although their likely sub-vertical orientation commonly inhibits their imaging so we cannot preclude their presence [see Magee and Jackson, 2020 and references therein].

For each interpreted intrusion, we measure their long axis, short axis, area, and transgressive height where applicable; these values should be considered minimum bounds as many intrusions thin towards their lateral tips and thus their measurement is limited by the resolution of the data [Eide et al., 2018; Magee et al., 2015]. We acknowledge human error may introduce further uncertainties into our measurements and thus conservatively consider they may have errors of up to 5%. Finally, without borehole information we cannot determine the absolute age of the intrusions. In some instances, we observe and describe vent-like features and intrusion-induced forced folds, which mark possible syn-intrusion palaeosurfaces and thus allow us determine the relative age of the associated intrusions [e.g., Trude et al., 2003]. Most intrusions are not associated with vents or forced folds, so we use the estimated age of the strata they were intruded into as a proxy for their maximum possible age of emplacement.

RESULTS

Salt seismic expression

The interpreted Base Salt (BS) corresponds to a complex and discontinuous stack of high-amplitude, commonly positive polarity reflection packages mapped between ~4.5–6.5 s TWT (e.g., Figs 2 and 3a). The Top Salt (TS) corresponds either to a high amplitude, positive polarity reflection or, where salt structures have vertical or overhanging margins, the transition between intra-salt chaotic reflections and sub-parallel reflections of the supra-salt sequence (e.g., Figs 2 and 3b). The salt itself is generally internally defined by chaotic, discontinuous, low-to-moderate reflections, particularly where it is thickest (e.g., Fig. 2). In places, the salt locally contains high-amplitude, more continuous reflections (e.g., Fig. 2).

Sub-salt structure

A key structural feature observed on the BS horizon is a linear, NNE-trending trough that marks the location of the underlying Merluza Graben (Figs 2 and 3a). The edges of the trough coincide with the upper tips of graben-bounding, inward-dipping, moderate throw (~0.2-0.5 s TWT) normal faults (Figs 2 and 3a). East of the Merluza Graben is a relatively flat-topped structural high (~4.5 s TWT tall), which is separated from a ~6.5 s TWT deep depocentre to the south by a large throw (~1 s TWT), ENE-WSW striking, S-dipping normal fault (Figs 3a and 4a). To the west of the Merluza Graben, the BS horizon is defined by a broad, relatively flat-topped terrace (Fig. 3a). The few dome-like structural highs on this terrace underlie salt structures and likely correspond to velocity pull-up artefacts (Figs 2 and 3a).

Salt structure

Our study area is characterized by variably oriented salt walls and stocks with variable orientations (Figs 3b and c). West of the Merluza Graben we observe ~20–30 km long, ~3–5 km wide, ENE-trending walls, which have with reliefs of up to ~3 s TWT (Figs 2, 3b and c). Stocks that are up to ~3–3.2 s TWT tall and ~1–2 km wide rise from low-relief (~0.5–1 s TWT) walls in this western area (Figs 2, 3b, c, and 4). These stocks have overhanging flanks and, locally, may be welded (e.g., Fig. 2a). East of the Merluza Graben, a ~10 km wide, >15 km long, and ~3.5s TWT tall wall is present (Figs 3b and c). Thin or nearly welded salt occurs below minibasins developed adjacent to the moderate to high-relief walls and stocks (Fig. 3c).

In contrast to the walls in the western and eastern portions of the study area, the two walls developed above the bounding faults of the Merluza Graben trend NNE-SSW, sub-parallel to the graben axis, and are ~15–30 km long, ~3 km wide, and 1–1.2 s TWT tall (Figs 3b and c). These two walls occur in the immediate footwall of and are bound on one side by salt-detached listric faults that dip away from the graben axis (e.g., Figs 2, 3b, c, and 4b). Given these diapirs are bound by and perhaps genetically related to salt-detached faults, we refer to them as salt rollers [sensu Bally, 1981; Brun and Mauduit, 2009]. The western roller is defined by a landward (west)-dipping fault that is up to ~2 s TWT tall and offsets the Cretaceous succession up to H5 (near Top Campanian) by ~0.5 s TWT (e.g., Figs 3b, c, and 4b). The eastern roller is bound by a basin-ward (east)-dipping, listric normal fault that is up to ~4.5 s TWT tall and offsets the Cretaceous and most of the Cenozoic succession, extending above H8 (intra-Neogene) by ~0.5–1 s TWT (e.g., Figs 3b, c, and 4b). A stock is developed near the Merluza Graben where the western roller intersects the eastern end of an ENE-WSW trending wall (Figs 3b and c). Within the limits of, and immediately above, the Merluza Graben, salt thickness broadly decreases northwards from ~1.45 to ~0.05 s TWT (Fig. 3c).

Supra-salt structure

The NNE-trending rollers developed above the edges of the Merluza Graben are associated with salt-detached faults containing very thick, wedge-shaped packages of growth strata in their hanging walls (Figs 4b and 5). For the western and eastern rollers, growth strata within their extensional rollovers are of Albian-to-Campanian (including H1-H5) and Albian-to-Neogene (including H1-H8) age, respectively (Figs 4b and 5). The greatest expansion indices, of 2.7 and 3.4 for the western and eastern faults, respectively, are recognised at H3 (Top Santonian) (Fig.

6); below and above H3, expansions indices for both faults are typically <1.5, except for H4 at the eastern fault where the expansion index is >2.5 (Fig. 6). The shared footwall of the roller-bounding, salt-detached faults is defined by a Albian-to-Santonian (TS-H3) minibasin, characterized by stratal thickening above a broad, sag-like depression in TS (Figs 4b and 5).

Away from the Merluza Graben and its overlying rollers, salt diapirs are flanked by 3–4 s TWT thick, Upper Cretaceous-to-Lower Cenozoic minibasins (Figs 2, 4c, and 5). Composite halokinetic sequences, defined by thinning and upturn of strata at the diapirs flanks [sensu Giles and Rowan, 2012; Pichel and Jackson, 2020], are present at the edges of these minibasins between H2 (near Coniacian-Santonian boundary) and H7 (intra-Paleogene) (e.g., Figs 2 and 4c). An earlier, Albian-to-Turonian (TS-H1) phase of longer-wavelength, minibasin-scale (> 1 km) folding and stratal thinning is observed adjacent to some of these stocks (Fig. 2b and 4c).

Igneous intrusions

Seismic expression and distribution of intrusions

We mapped 38 intrusions in the 3D seismic reflection data, with 18 located above the salt (S1-S18), 18 within the salt (S19-S36), and two below the salt (S37-S38) (Fig. 6). Each intrusion corresponds to high-amplitude, positive-polarity, tuned reflection packages (e.g., Figs 2, 3, 7, and 8). The intrusions are laterally discontinuous and typically appear circular-to-elliptical in plan-view (e.g., Figs 2, 3, 7, and 8). We classify intrusions as either sub-horizontal sills, saucer-shaped sills, or inclined sheets (e.g., Figs 2, 3, 7, and 8). Saucer-shaped sills display inwardly inclined limbs that fully or partially encompass (i.e. they have arcuate strikes) and extend upwards from a flat or inclined inner sills (e.g., S1 and S10; Figs 8a and b). Inclined sheets may also extend upwards from a small sill, but these are planar rather than arcuate (e.g., S13; Fig. 8c).

Of the 18 intrusions that occur within the Cretaceous strata above TS, the majority (14; S1-S14) occur along a ~10 km wide, N-trending zone situated above the Merluza Graben (Figs 8a-c). Intrusions above the Merluza Graben are only observed where salt thickness is ~<1 s TWT (Fig. 3c and 7d). Two intrusions (S15-S16) above TS are located ~5 km to the west of the Merluza Graben, whereas S17 and S18 are located ~5 km to the east, where the salt is <0.5 s TWT thick (Figs 7a and d). Intrusions above TS display either saucer-shaped (S1-S10, S17) or inclined sheet (S11-S16, S18) morphologies (Figs 2, 4b, 7b-c, and 8; Table 1); of the seven inclined sheets, seismic-stratigraphic relationships reveal two (S12-S13; e.g., Fig. 8c) are concordant with dipping strata and four (S14-S16, S18) are transgressive (e.g., Fig. 2). Parts of S17 and S18 coincide with the TS horizon where it is faulted against syn-kinematic stratal packages (e.g., Fig. 2b). Two intrusions (S17-S18) are confined to strata between TS and H1 (near Cenomanian-Turonian boundary), whereas 15 intrusions (S2-S16) predominantly located within this stratal package extend above H1 (e.g., Figs 2, 4b, and 8c). One intrusion, a saucer-shaped sill (S1), is located above H2 (near Coniacian-Santonian boundary) (Fig. 8a).

Of the 18 intrusions that primarily occur within the salt, seven (S19-S25) are hosted by a NW-trending wall near the southern limits of the Merluza Graben (Figs 7a, d, and e); the upper tip of S21 extends above TS into the overlying Cretaceous strata. Most other intra-salt intrusions occur beneath the flanks of stocks west of the Merluza Graben (Fig. 7d). S33 is located at the edge of a large salt wall to the east of the Merluza Graben, whereas S32 and S34 are situated within a <0.5 s TWT thick portion of a salt roller (Figs 4a and 7d). We describe four intra-salt sills as saucer-shaped (S19, S21, S32, and S34), two as sub-horizontal (S26-S27), and 12 as inclined sheets (S20, S22-S25, S28-S29, S31, S33, and S35-S36) (e.g., Figs 2, 4a, and b; Table

1). We map two transgressive sills (S37-S38) below the salt (Figs 7a and e); these both extend upwards into and terminate within the salt.

The tuned reflection packages representing the supra-salt intrusions are commonly segmented by local variations in amplitude and dip (e.g., Figs 8a and b); intra-salt intrusions do not appear to be similarly segmented (e.g., Figs 2, 4b, and 8). Aside from marking the transition from the inner sill to inclined limbs within saucer-shaped intrusions, changes in dip typically correspond to abrupt, yet small (typically <0.05 s TWT high), vertical offsets in reflections where host rock strata is transgressed (e.g., Figs 8a and b). Although the distribution of these linear steps is commonly complex, they tend to occur either parallel to the strike of transgressive sheets (e.g., Fig. 8a) or radiate outwards from the deepest portion of a sill (e.g., Fig. 8b). Amplitude variations are also complex but numerous intrusions display arrays of linear, high-amplitude zones adjacent, and parallel, to the small vertical offsets (e.g., Figs 8a and b); some linear high amplitude zones occur independent of changes in reflection dip, particularly around the outer edges of saucer-shaped sills.

Quantitative intrusion analysis

The 38 mapped intrusions have long axes ranging from 1.64–6.42 km, and areas of 1.28–27.85 km^2. Intrusion aspect ratios vary from 1.06–2.78, with a mean of 1.64 and standard deviation of 0.44, indicating most are sub-circular (Table 1). Although we define three distinct intrusion populations based on their stratigraphic relationship to the salt (i.e. sub-salt, intra-salt, and supra-salt), there is little difference in their geometrical properties (Fig. 9). For example, cross-plotting long axes length, intrusion height, area, and aspect ratio reveals all intrusion populations overlap and display similar trends (Fig. 9). A notable exception is that the four largest intrusions, in terms of their long axis and area, occur above TS (i.e. S8, S10, S12, and S17; Fig. 9 and Table 1). Supra-salt intrusion transgressive height is moderately-to-strongly, positively correlated with both area and long axis (R^2 = 0.60 and 0.55, respectively), as is the relationship between long axis and area (R^2 = 0.8); intra-salt intrusions display similar but typically weaker, positive trends (R^2 = 0.25–0.89) (Figs 9a, c, and d). Aspect ratios of both intra-and supra-salt sills show no correlation to area or long axis length (R^2 = 0.12; Figs 9b and e).

Structures spatially associated with intrusions

Reflections immediately overlying the mapped intrusions are typically not locally folded (Figs 2, and 4). However, the strata above S4 and S5 are deformed into a ~6 km wide, ~0.1 s TWT high, dome-shaped fold (e.g., Fig. 4b). The reflection marking the top of this fold, located just above H2 (near Coniacian-Santonian boundary), truncates underlying reflections and is onlapped by overlying strata (e.g., Fig. 4b). This dome-shaped fold is superimposed onto a broader area (~192 km^2) of locally elevated relief expressed across H2 and H3 (near Top Santonian) above the Merluza Graben (Figs 4b, 5b, and c). Underlying this area of elevated relief are the supra-salt intrusions S2-S7, S9-S11, and S15. Strata between H3 and H6 (near Top Cretaceous) thin across this area of elevated relief (Fig. 5d).

In the supra-salt strata above the Merluza Graben, we identify three vent-like structures (e.g., Figs 4b and 8c). Two vent-like structures (V1 and V2) display a complex eye-shaped morphology; they are bound by convex-downwards bases, which truncate stratigraphic reflections, and irregular, convex-upwards tops that are onlapped by overlying strata (e.g., Fig. 8c. The oldest of these vent-like structures (V1) is onlapped by H2 and cross-cut by the younger eye-shaped feature (V2), which is itself onlapped by intra-Santonian strata (e.g., Fig. 8c).

Seismic amplitude is variable across the surfaces bounding these eye-shaped structures, but is typically low and increases at the edges of the structures where they merge (e.g., Fig. 8c). The upper surface reflections most commonly have a negative polarity, with rarer occurrences displaying a positive polarity (e.g., Fig. 8c). Basal surface reflections are positive polarity (e.g., Fig. 8c). Reflections within the eye-shaped structures also vary in amplitude, although they are typically low-amplitude, and are chaotic (e.g., Fig. 8c). The third vent-like structure (V3) rests on directly on the lateral limit of the fold developed above S4 and S5 (Fig. 4b). Unlike V1 and V2, V3 displays a conformable base onto which convex-upwards reflections downlap; the uppermost of the convex-upwards reflections is onlapped by overlying strata (Fig. 4b).

DISCUSSION

Timing of salt tectonics

Onlap of Albian-to-Santonian strata (including H1-H3) onto stocks, as well as ENE-to-NE-trending walls and rollers, coupled with the presence of associated salt-detached growth faults, indicate salt movement started soon after its deposition in the Late Aptian-to-Early Albian (Figs 2 and 4). These seismic-stratigraphic observations are consistent with previous studies that linked Albian-to-Cenomanian salt deformation to gravity driven, up-dip extension generated by margin tilting (Figs 1b, c, and 2) [e.g., Davison et al., 2012; Demercian et al., 1993; Quirk et al., 2012]. Halokinetic sequences observed in minibasins away from the Merluza Graben, and located between H2 (near Coniacian-Santonian boundary) and H7 (intra-Paleogene), suggests adjacent stocks and walls rose as passive diapirs during the Late Cretaceous-to-Early Cenozoic (e.g., Figs 2 and 4) (e.g., Coleman et al., 2018). The presence of secondary welds and diapirs with tear-drop shaped cross-sectional geometries, coupled with folding and uplift of diapir roofs, indicates active diapir rise until the Neogene, and suggests deformation up-dip of the Merluza

Graben was influenced by late-stage shortening (e.g., Figs 2 and 4C) (e.g., Coleman et al., 2018). Compared to elsewhere along the up-dip extensional domain, this late-stage shortening landwards of the Merluza Graben appears localised to our study area [e.g., Davison et al., 2012; Quirk et al., 2012].

In contrast to the extension- and contraction-driven growth of very large (up to ~3.2 s TWT tall) salt structures away from the Merluza Graben, the rollers above its bounding faults are ~1.2 s TWT tall and only display evidence of extension-driven, Albian-to-Campanian or Albian-to-Neogene growth (Figs 2, 4, and 6); i.e. rollers above the Merluza Graben *did not* evolve into passive or subsequently active diapirs. Deformation of the rollers was preferentially accommodated by slip and rollover of overburden strata above associated normal faults, generally decreasing through time after its peak during the Santonian (Figs 4b and 6). Furthermore, the relative increase in thickness of Albian-to-Santonian growth strata above the northern sector of the Merluza Graben, compared to some other parts of the study area, suggests salt movement and accommodation generation were locally enhanced during this period (e.g., Fig. 2, 4a and 5e).

Timing of igneous activity

A variety of igneous events have been recognised in the Santos Basin, including Early Cretaceous pre-rift and syn-rift magmatism, pre-salt volcanism, and post-salt magmatic activity, which are mainly dated as Santonian and Eocene [e.g., Fornero et al., 2019; Oreiro et al., 2008]. Because the igneous intrusions and associated extrusive features we map are not intersected by boreholes, we cannot constrain their emplacement age using radiometric techniques. However, we note that the presence of intrusions within a stratigraphic package indicates emplacement occurred during or after its deposition; i.e. borehole-derived biostratigraphic dates of strata hosting intrusions can thus be used to define the maximum emplacement age. To estimate the maximum emplacement age of intrusions hosted within the Cretaceous strata, we examined the youngest mapped stratigraphic horizon they cross-cut. For example, although S37 and S38 are primarily sub-salt, they transgress BS and their emplacement must therefore post-date salt deposition; i.e. magmatism occurred post-earliest Albian. Similarly, we identify one saucer-shaped sill (S1) emplaced above H2 (i.e. the near Coniacian-Santonian boundary) that terminates just below H3, near the Top Santonian, suggesting at least some magmatic activity occurred towards the end of the Santonian or later. By only assessing the age of the host rock encasing intrusions, we cannot determine whether all magmatic activity occurred simultaneously (e.g., towards the end of the Santonian), or if intrusion was incremental over a prolonged period of time (e.g., between the early Albian and end Santonian) [e.g., Magee et al., 2014; Reeves et al., 2018; Trude et al., 2003].

To further constrain the age of magmatic activity, we note there is a dome-shaped fold developed directly above S4 and S5 (e.g., Fig 4b), which we suggest formed to accommodate the intruded magma volume; i.e. it is an intrusion-induced forced fold [e.g., Hansen and Cartwright, 2006; Magee et al., 2013a; Stearns, 1978; Trude et al., 2003]. The top of this fold occurs just above H2, where it truncates underlying reflections and is onlapped by overlying, likely of the earliest Santonian strata (Fig. 4b). These seismic-stratigraphic relationships indicate the top fold surface marked the syn-intrusion palaeosurface [cf. Trude et al., 2003], suggesting S4 and S5 were emplaced in the Santonian. The presence of stacked, convex-upwards reflections (V3) downlapping onto this folded horizon appear similar to volcanoes and hydrothermal vents observed elsewhere, further supports our inference that the top fold marked a syn-intrusion palaeosurface (Fig. 4b) [e.g., Hansen, 2006; Magee et al., 2013b; Reynolds et al., 2018]. As S1 occurs at a higher stratigraphic level than the Santonian reflections that onlap the forced fold, it is thus younger than S4 and S5 (Fig. 8a).

We identify several eye-shaped structures within our data, which have tops located at and onlapped by different stratigraphic horizons; i.e. V1 is onlapped by H2, whilst V2 is onlapped by intra-Santonian strata (e.g., Fig. 8c). These eye-shaped structures appear similar to hydrothermal vents observed in seismic reflection data elsewhere [e.g., Jamtveit et al., 2004; Magee et al., 2016a; Planke et al., 2005; Svensen et al., 2003]. If the eye-shaped structures mapped are related to magmatism in the study area, their development at different stratigraphic levels further implies igneous activity was punctuated. Overall, based on our seismic-stratigraphic observations, we suggest igneous activity likely initiated after salt deposition and the onset of salt movement, probably during the Albian-to-Turonian. Magmatism continued, albeit likely incrementally, to the late Santonian or later. Our inferred ages of igneous activity broadly coincide with a phase of widespread magmatism across the Santos and Campos basins at ~90–80 Ma [e.g., Oreiro et al., 2008]; a magmatic event at this time is supported by the high percentage of altered basalt fragments within Santonian turbidite reservoirs across the Santos Basin [e.g., Klarner et al., 2008; Mohriak, 2003]. With respect to the salt-related deformation history outlined above, Albian-to-Santonian magmatism implies intrusion occurred synchronous to gravity driven salt tectonics (Fig. 1b).

Salt-magma interaction

Influence of salt on magma emplacement mechanics

The geometry, size, and distribution of igneous sheet intrusions is influenced by the physical behaviour of the host rock during magma emplacement [e.g., Gudmundsson, 2011; Kavanagh et al., 2006; Kavanagh and Pavier, 2014; Magee et al., 2016b; Schmiedel et al., 2017; Schmiedel et al., 2019; Schofield et al., 2014; Schofield et al., 2012]. Whilst sheet intrusions are typically considered to propagate via brittle tensile fracturing of host rock, several studies have demonstrated sill emplacement can also be facilitated by host rock fluidisation, ductile flow, and/or viscous indentation [Galland et al., 2019; Pollard et al., 1975; Schofield et al., 2014; Spacapan et al., 2017]. For example, Schofield et al. [2014] showed mafic magma emplaced within the Werra salt complex (Herfa-Neurode mine, Germany) intruded via (e.g., Fig. 10): (i) brittle fracturing within halite sequences, forming dykes; and (ii) non-brittle, fluidisation of sub-horizontal carnallite layers, where magma was emplaced as sills. These variations in intrusion geometry and emplacement mechanics likely reflect differences in the temperature-dependent behaviour of halite and carnalite; halite is anhydrous and melts at ~800°C, whereas carnallite is hydrous and behaves as a viscous fluid when it dehydrates at ~140–170°C [Schofield et al., 2014]. The thermal conductivity of halite (6.1 W $m^{-1}°C^{-1}$) and carnallite (0.8 W $m^{-1}°C^{-1}$) may also have affected magma emplacement mechanics as the rapid transfer of heat into rocks with high thermal conductivities will inhibit their melting [Schofield et al., 2014]. Overall, it seems likely that salts with relatively high melting temperatures and thermal conductivities (e.g., halite, sylvite, and anhydrite) will fracture during rapid (i.e. high strain rate) magma emplacement, whereas those with low dehydration temperatures and thermal conductivities (e.g., carnallite, epsomite, gypsum, bischofite, and kieserite) may behave as a fluid during intrusion and thus deform in a non-brittle fashion [Schofield et al., 2014].

Due to a lack of borehole data we do not know the composition or distribution of different evaporites within the salt structures mapped in our study area. Furthermore, seismic reflection data is unable to resolve the small-scale features (e.g., intrusion tip geometry) indicative of different magma emplacement processes [see Magee et al., 2019 and references therein]. Despite these limitations in our data, we make several observations that may provide some insight into whether the syn-emplacement behaviour of the salt affected magma intrusion. We first note that many supra-salt intrusion reflections are characterised by arrays of subtle but abrupt, linear vertical offsets (e.g., Figs 2, 4b, 8a, and b). These vertical offsets are oriented either parallel to the strike of inclined sheets, or saucer-shaped sill limbs (e.g., Fig. 8a), or are radially disposed around a deep portion of the intrusion (e.g., Fig. 8b). Where similar vertical offsets have been observed in outcrop, structural relationships and petrofabric data reveal these features commonly develop in response to the formation, and potential coalescence, of vertically offset sheet segments during propagation [e.g., Magee et al., 2019; Walker, 2016]. In contrast to the supra-salt sills, those emplaced within the salt are expressed as apparently smoother reflections; i.e. they appear to contain relatively fewer, abrupt vertical offsets (e.g., Figs 2, 4a, b, and 8). This smoother appearance of the intra-salt sills may imply that they were emplaced either as: (i) continuous (i.e. they were not segmented) sheets; or (ii) closely spaced magma fingers, which tend to form (although not always) at the same structural level, in response to non-brittle deformation of the host salt rock (e.g., fluidisation) [e.g., Galland et al., 2019; Pollard et al., 1975; Schofield et al., 2010].

We do not have the hard rock data to test our speculations, but the apparent variation in reflection smoothness between the intra-and supra-salt sills suggest the differences in their respective host rock may have influenced emplacement mechanics. Although we postulate intra-and supra-salt sill emplacement may have been mechanically different, all intrusion populations are geometrically similar (Fig. 9). This lack of geometrical variation across the intrusions suggests their size may have been primarily controlled by emplacement depth and stress conditions, as opposed to the host rock lithology [e.g., Fialko et al., 2001; Menand, 2011; Pollard and Johnson, 1973](e.g., Pollard and Johnson, 1973; Fialko and Simons, 2001; Menand, 2011).

Influence of salt on magma distribution

Intra-salt intrusions, including those clustered above the Merluza Graben and its western bounding fault, are observed in the salt where it is relatively thin (~<1 s TWT thick), typically <0.5 s TWT thick (Figs 2, 4, 7d and 8). Diapirs >1.5 s TWT thick appear to lack intrusions within them, although some intra-salt sills are observed close to their flanks (Figs 2, 4c and 7d). This apparent absence of intrusions in the large salt structures may be real, or it may reflect that sub-horizontally emplaced sills were rotated to steeper dips during diapir growth, inhibiting their imaging by seismic reflection data. Most supra-salt intrusions are interconnected (i.e. they form a sill-complex) and occur within and along the Merluza Graben, where the underlying salt is relatively thin (~<1 s TWT thick), away from areas containing intra-salt sills (e.g., Fig. 7). The distribution of the intra- and supra-salt intrusions, including the location of sub-salt sills, implies: (i) the pre-salt Merluza Graben likely focused Albian-to-Santonian magma ascent, consistent with observations from elsewhere in the Santos Basin that pre-rift structures directed post-rift magmatism [e.g., Mohriak et al., 1995; Oreiro et al., 2008]; and (ii) intrusions emplaced within the salt rarely fed supra-salt sills or inclined sheets. The lack of observed feeders to the supra-salt sill-complex above the Merluza Graben (e.g., Fig. 7d) suggests it was likely fed by dykes that are not imaged by our seismic reflection data, perhaps because their sub-vertical contacts reflected little or no seismic energy back to the surface [e.g., Eide et al., 2018; Magee and Jackson, 2020; Malehmir et al., 2018]. If dykes did feed the supra-salt sill-complex, their bypassing of the salt during ascent may indicate the underlying evaporites are dominated halite [e.g., units A1 or A3; Rodriguez et al., 2018], which can fracture at high strain rates to accommodate dyking because it has a relatively high melting temperature and thermal conductivity [cf. Schofield et al., 2014]. In contrast, we suggest that where the salt contains, or contained, evaporites (e.g., carnallite) with low dehydration temperatures and thermal conductivities [e.g., units A2 or A4; Rodriguez et al., 2018], space generated by their dehydration during emplacement may have favoured sill formation and arrested magma ascent [cf. Schofield et al., 2014].

Influence of magmatism on the tectono-stratigraphic development of salt basins

We show that Albian-to-Santonian magmatism coincided with the main phase of salt movement (Figs 2 and 4). At this time, localised growth of Albian-to-Santonian strata towards the extensional rollovers above the Merluza Graben accommodated more deformation in the area relative to the rise of neighboring walls and diapirs; i.e. suggesting salt flow and related deformation was greatest where magma was being emplaced (Figs 2-4, 7, and 11). Albian-to-Santonian salt movement above the Merluza Graben may have been instigated by (Figs 11a and b): (i) the presence of an inherited base-salt low, containing thicker, more halite-rich, and thus more mobile salt than adjacent areas [e.g., Dooley et al., 2017; Dooley et al., 2020; Pichel et al., 2019a; Pichel et al., 2019b]; and/or (ii) heat-enhanced salt flow driven by igneous activity within the Merluza Graben [Schofield et al., 2014; Underhill, 2009].

In addition to the potential role of magmatism in driving salt movement, we identify an anomalous area of elevated structural relief expressed at H2 (near Coniacian-Santonian boundary) and H3 (near Top Santonian) above the supra-salt sill-complex in the Merluza Graben (e.g., Figs 4b, 5b, and c). This zone of uplift corresponds to a NW-trending antiform and occurs within the shared footwall of the two, NE-SE striking, outward-dipping, salt-detached faults overlying a top-salt low above the Merluza Graben (e.g., Figs 4b, 5b, and c). Strata between H1 (near Cenomanian-Turonian boundary) and H3 thicken across this antiform, whilst strata bound by H3 and H6 (near Top Cretaceous) thins across the structure (Figs 5e and f). We suggest emplacement of sills, some of which may not be resolved in our seismic reflection data, within the Albian-to-Santonian sedimentary sequence, locally led to the over-thickening of strata as the magma volume was accommodated by roof uplift and/or floor subsidence (Fig. 11c) [Mark et al., 2019].

Post-Santonian (i.e. post-intrusion) salt-induced deformation can be sub-divided into two distinct structural domains in our study area: (i) west of the Merluza Graben where the salt, resting on a relatively undeformed terrace, rised diapirically by passive processes, followed by late-stage, Cenozoic shortening and active rise (e.g., Figs 2, 3a, and 11d); and (ii) above the Merluza Graben, where diapirism was driven by continued, albeit decreasing, extension on salt-detached listric normal faults and limited diapiric salt rise (e.g., Figs 2, 3a, 4b, 6, and 11d. This post-Santonian strain partition, with up-dip shortening and coeval down-dip extension, coupled with significant variations in the degree of salt rise, could, in places, be attributed to welding of the salt layer between the up-dip diapirs. However, such welding could not explain the strain-partition in areas where the salt layer is still relatively thick (~>200 ms TWT) and, thus, up-dip diapirs are still connected with the salt structures down-dip in the Merluza Graben (e.g., Fig. 2b). Alternatively, strain partitioning may have been driven by base-salt relief within the pre-salt Merluza Graben as its western shoulder could have acted as a local barrier to basin-ward salt flow and promoted mild up-dip shortening, similar to other areas in the Santos Basin [Dooley et al., 2020; Pichel et al., 2019a; Pichel et al., 2019b]. However, it is unclear why graben-related buttressing would have led to strain partitioning in the post-Santonian, after most salt had been evacuated from beneath the minibasins, and not before [Jackson and Hudec, 2017; Peel, 2014; Pichel et al., 2018]. Post-intrusion salt movement could also be restricted by [Schofield et al., 2014]: (i) the presence of mechanically strong crystalline intrusions within the salt, forming a rigid framework that buttressed salt movement; and (ii) the syn-intrusion dehydration of weak evaporite layers (e.g., gypsum and carnallite), which commonly lubricate salt movement, compared to stronger counterparts, such as anhydrite and halite [e.g., Jackson and Hudec, 2017; Urai et al., 1986; Van Keken et al., 1993].

CONCLUSIONS

Salt tectonics and magmatism are prevalent in many sedimentary basins worldwide. It is thus inevitable that, in some places, magma will interact with salt rocks as it ascends towards the surface. We use 3D seismic reflection data from the Santos Basin, offshore Brazil to examine the interactions between igneous sheet intrusions emplaced below, within, and above an Aptian salt layer. Sills are geometrically similar regardless of whether they were emplaced below, within, or above the salt, although those within the salt intrusion are characterised by smoother reflections. We also observe intra-salt and supra-salt sill clusters to be laterally offset and not linked. We suggest some areas of the salt captured ascending magma, perhaps because they contained hydrous salts that favoured sill emplacement, whilst other areas were bypassed by dyke intrusion. Mapping of salt structures and halokinetic sequences reveals salt movement began in the Albian-to-Santonian due to gravity driven extension. This Albian-to-Santonian phase of salt movement was primarily focused above the pre-salt Merluza Graben where salt rollers developed with listric normal faults in the sedimentary cover. Seismic-stratigraphic analyses of onlaps onto intrusion-induced forced folds and vents indicates sill emplacement, which was focused above the Merluza Graben, coincided with this Albian-to-Santonian phase of salt movement. Post-Santonian salt movement above the Merluza Graben continued via extensional roll-over with little salt rise, albeit at a decreased rate, but elsewhere was dominated by active and/or passive diapir ascent. We suggest the intrusion of hot magma enhanced salt flow during the Albian-to-Santonian, localising salt movement above the Merluza Graben, but upon crystallisation formed a rigid intrusive framework within the salt that inhibited Post-Santonian salt rise. Overall, our results suggest salt-magma interactions influenced magma emplacement mechanics and intrusion distribution, whilst the presence of hot magma and crystallised intrusions within the salt impacted salt tectonics.

FIGURE CAPTIONS

Figure 1: (**a**) Location map of the Santos Basin offshore Brazil, highlighting relevant tectonic and salt-related domains [modified from Davison et al., 2012; Jackson et al., 2015a]. (**b**) Tectono-stratigraphic column showing mapped seismic horizons [Duarte and Viana, 2007; Jackson et al., 2015a; Modica and Brush, 2004]. (**c**) Geoseismic section depicting the passive margin structure of the Santos Basin and the location of the extensional, translational, and contractional domains [modified from Davison et al., 2012; Jackson et al., 2015a]. See Figure 1a for location.

Figure 2: (**a**-**b**) Uninterpreted and interpreted, time-migrated seismic sections across the study area showing a sample of the different salt structures, halokinetic sequences, and intrusions present. See Figure 3 for line locations.

Figure 3: Time-structure maps of the (**a**) Base Salt and (**b**) Top Salt horizons, and (c) an isochore map showing the vertical thickness in time between the Base and Top Salt horizons. Salt structure distribution is interpreted in (**c**).

Figure 4: (**a**-**c**) Uninterpreted and interpreted, time-migrated seismic sections across the study area showing a sample of the different salt structures, halokinetic sequences, and intrusions present. An inferred vent associated with sill emplacement is shown in (**b**). See Figure 2 for key and Figure 3 for line locations.

Figure 5: (**a-d**) Time-structure maps of H1, H2, H3, and H6. (**e-f**) Isochore thickness maps for the Top Santonian-to-Top Salt horizons and the Top Cretaceous-to-Top Santonian horizons, respectively.

Figure 6: Expansion index plots for the western and eastern listric faults above the Merluza Graben.

Figure 7: (**a**) Map of sill outlines highlighting those observed below, within, and above the salt. (**b**) Supra-salt sill time-structure maps shown above the Top Salt horizon time-structure map. (**c**) Oblique 3D view of (**b**). Vertical exaggeration = VE. (**d**) Sill outline maps overlaid onto salt

isochore map. (**e**) Intra-salt sill time-structure maps shown above the Base Salt horizon time-structure map. (**f**) Sub-salt sills beneath the Base Salt horizon.

Figure 8: (**a**-**c**) Interpreted seismic sections showing examples of sills and inferred vents in the study area; see Supplementary Figure 1 for uninterpreted sections. Time-structure maps, as well as combined Root-mean squared (RMS) amplitude and dip maps, highlight the plan-view geometry of key sills.

Figure 9: Cross-plots of different sill geometrical parameters highlighting little difference between the structure of those intrusions below, within, and above the salt.

Figure 10: Schematic showing salt-magma interactions in the Werra salt, Germany [redrawn from Schofield et al., 2014]. The mafic magma intruded as dykes within halite, but fluidised carnallite layers where it formed sills [Schofield et al., 2014].

Figure 11: Schematics showing the possible salt tectonic and magmatic evolution of the study area. (**a**) In the Aptian, salt was deposited over a rugged topography, including the pre-salt Merluza Graben. (**b**) Near the Cenomanian-Turonian boundary, after salt deposition, salt flow towards the east led to passive diapirism and development of rollers in the study area; the rollers occur in the footwall of extensional, salt-detached faults located above the boundaries of the Merluza Graben. Magmatism above the Merluza Graben produced discrete intra- and supra-salt sill-complexes. (**c**) At the end Santonian, magmatism had ceased, resulting in a crystallised rigid framework of intrusions within the salt and younger Cretaceous strata above the Merluza

Graben. (**d**) In the Cenozoic, up till in the Neogene, salt kinematics up-dip of the Merluza Graben was locally characterised by shortening and active diapirism, produced teardrop-shaped salt bodies. Extension continued above the Merluza Graben on the east-dipping salt-detached fault. (**d**). General section structure based on Figure 2a.

REFERENCES

Bally, A. (1981). Thoughts on the tectonics of folded belts. In K. McClay and N. Price (Eds.), *Thrust and Nappe Tectonics* (Vol. 9, pp. 13-32). London: Geological Society, London, Special Publications.

Barton, M. D., and D. A. Johnson. (1996). "Evaporitic-source model for igneous-related Fe oxide–(REE-Cu-Au-U) mineralization". *Geology 24*(3), pp. 259-262.

Bedard, J. H., H. R. Naslund, P. Nabelek, A. Winpenny, M. Hryciuk, W. Macdonald, . . . E. Girard. (2012). "Fault-mediated melt ascent in a Neoproterozoic continental flood basalt province, the Franklin sills, Victoria Island, Canada". *Geological Society of America Bulletin 124*(5-6), pp. 723-736.

Blažić, L., and J. Moreau. (2017). "Discovery of Lower Cretaceous hydrothermal vent complexes in a late rifting setting, southern North Sea: insights from 3D imaging". *Journal of the Geological Society 174*(2), pp. 233-241.

Brown, A. R. (2011). *Interpretation of three-dimensional seismic data* (6th ed. Vol. 42). Oklahoma, USA: AAPG and SEG.

Brun, J.-P., and T. P.-O. Mauduit. (2009). "Salt rollers: Structure and kinematics from analogue modelling". *Marine and petroleum geology 26*(2), pp. 249-258.

Davison, I., L. Anderson, and P. Nuttall. (2012). Salt deposition, loading and gravity drainage in the Campos and Santos salt basins. In G. Alsop, S. Archer, A. Hartley, G. NT, and R. Hodgkinson (Eds.), *Salt Tectonics, Sediments, and Prospectivity* (Vol. 363, pp. 159-174). London: Geological Society, London, Special Publications.

Demercian, S., P. Szatmari, and P. Cobbold. (1993). "Style and pattern of salt diapirs due to thin-skinned gravitational gliding, Campos and Santos basins, offshore Brazil". *Tectonophysics 228*(3-4), pp. 393-433.

Dooley, T. P., M. R. Hudec, D. Carruthers, M. P. Jackson, and G. Luo. (2017). "The effects of base-salt relief on salt flow and suprasalt deformation patterns—Part 1: Flow across simple steps in the base of salt". *Interpretation 5*(1), pp. SD1-SD23.

Dooley, T. P., M. R. Hudec, L. M. Pichel, and M. P. Jackson. (2020). The impact of base-salt relief on salt flow and suprasalt deformation patterns at the autochthonous, paraautochthonous and allochthonous level: insights from physical models. In K. McClay and J. Hammerstein (Eds.), *Passive Margins: Tectonics, Sedimentation and Magmatism* (Vol. 476, pp. 287-315). London: Geological Society, London, Special Publications.

Duarte, C. S., and A. R. Viana. (2007). Santos Drift System: stratigraphic organization and implications for late Cenozoic palaeocirculation in the Santos Basin, SW Atlantic Ocean. In A. Viana and M. Rebesco (Eds.), *Economic and Palaeoceanographic Significant of Contourite Deposits* (Vol. 276, pp. 171-198). London: Geological Society, London, Special Publications.

Eide, C. H., N. Schofield, I. Lecomte, S. J. Buckley, and J. A. Howell. (2018). "Seismic Interpretation of Sill-complexes in Sedimentary Basins: The 'sub-sill Imaging Problem'". *Journal of the Geological Society 175*, pp. 193-209.

Fialko, Y., Y. Khazan, and M. Simons. (2001). "Deformation due to a pressurized horizontal circular crack in an elastic half-space, with applications to volcano geodesy". *Geophysical Journal International 146*(1), pp. 181-190.

Fornero, S. A., G. M. Marins, J. T. Lobo, A. F. M. Freire, and E. F. de Lima. (2019). "Characterization of subaerial volcanic facies using acoustic image logs: Lithofacies and log-facies of a lava-flow deposit in the Brazilian pre-salt, deepwater of Santos Basin". *Marine and petroleum geology 99*, pp. 156-174.

Galland, O., J. B. Spacapan, O. Rabbel, K. Mair, F. G. Soto, T. Eiken, . . . H. A. Leanza. (2019). "Structure, emplacement mechanism and magma-flow significance of igneous fingers–Implications for sill emplacement in sedimentary basins". *Journal of Structural Geology 124*, pp. 120-135.

Giles, K. A., and M. G. Rowan. (2012). Concepts in halokinetic-sequence deformation and stratigraphy. In G. Alsop, S. Archer, A. Hartley, G. NT, and R. Hodgkinson (Eds.), *Salt Tectonics, Sediments and Prospectivity* (Vol. 363, pp. 7-31). London: Geological Society, London, Special Publications.

Gudmundsson, A. (2011). "Deflection of dykes into sills at discontinuities and magma-chamber formation". *Tectonophysics 500*(1-4), pp. 50-64.

Guerra, M. C., and J. R. Underhill. (2012). Role of halokinesis in controlling structural styles and sediment dispersal in the Santos Basin, offshore Brazil. In G. Alsop, S. Archer, A. Hartley, G. NT, and R. Hodgkinson (Eds.), *Salt Tectonics, Sediments, and Prospectivity* (Vol. 363, pp. 175-206). London: Geological Society, London, Special Publications.

Hansen, D. M. (2006). "The morphology of intrusion-related vent structures and their implications for constraining the timing of intrusive events along the NE Atlantic margin". *Journal of the Geological Society 163*, pp. 789-800.

Hansen, D. M., and J. Cartwright. (2006). "The three-dimensional geometry and growth of forced folds above saucer-shaped igneous sills". *Journal of Structural Geology 28*(8), pp. 1520-1535.

Heimdal, T. H., S. Callegaro, H. H. Svensen, M. T. Jones, E. Pereira, and S. Planke. (2019). "Evidence for magma–evaporite interactions during the emplacement of the Central Atlantic Magmatic Province (CAMP) in Brazil". *Earth and Planetary Science Letters 506*, pp. 476-492.

Holford, S. P., N. Schofield, J. D. MacDonald, I. R. Duddy, and P. F. Green. (2012). "Seismic analysis of igneous systems in sedimentary basins and their impacts on hydrocarbon prospectivity: examples from the southern Australian margin". *APPEA Journal 52*, pp. 23.

Hudec, M. R., and M. Jackson. (2007). "Terra infirma: Understanding salt tectonics". *Earth-Science Reviews 82*(1), pp. 1-28.

Iacono-Marziano, G., C. Ferraina, F. Gaillard, I. Di Carlo, and N. T. Arndt. (2017). "Assimilation of sulfate and carbonaceous rocks: experimental study, thermodynamic modeling and application to the Noril'sk-Talnakh region (Russia)". *Ore Geology Reviews 90*, pp. 399-413.

Jackson, C. A.-L., M. P. Jackson, and M. R. Hudec. (2015a). "Understanding the kinematics of salt-bearing passive margins: A critical test of competing hypotheses for the origin of the Albian Gap, Santos Basin, offshore Brazil". *Geological Society of America Bulletin 127*(11-12), pp. 1730-1751.

Jackson, C. A.-L., M. P. Jackson, M. R. Hudec, and C. R. Rodriguez. (2015b). "Enigmatic structures within salt walls of the Santos Basin—Part 1: Geometry and kinematics from 3D seismic reflection and well data". *Journal of Structural Geology 75*, pp. 135-162.

Jackson, M. (1995). Retrospective salt tectonics. In M. Jackson, D. Roberts, and S. Snelson (Eds.), *Salt Tectonics: A Global Perspective* (Vol. 65, pp. 1-28): AAPG Memoir.

Jackson, M. P., and M. R. Hudec. (2017). *Salt tectonics: Principles and practice*. Cambridge: Cambridge University Press.

Jamtveit, B., H. Svensen, Y. Y. Podladchikov, and S. Planke. (2004). "Hydrothermal vent complexes associated with sill intrusions in sedimentary basins". *Physical geology of high-level magmatic systems 234*, pp. 233-241.

Karner, G., and L. Gambôa. (2007). Timing and origin of the South Atlantic pre-salt sag basins and their capping evaporites. In B. Schreiber, S. Lugli, and M. Babel (Eds.), *Evaporites Through Space and Time* (Vol. 285, pp. 15-35). London: Geological Society, London, Special Publications.

Kavanagh, J. L., T. Menand, and R. S. J. Sparks. (2006). "An experimental investigation of sill formation and propagation in layered elastic media". *Earth and Planetary Science Letters 245*(3-4), pp. 799-813. DOI: 10.1016/j.epsl.2006.03.025

Kavanagh, J. L., and M. J. Pavier. (2014). "Rock interface strength influences fluid-filled fracture propagation pathways in the crust". *Journal of Structural Geology 63*, pp. 68-75.

Klarner, S., B. Ujetz, and R. L. Fontana. (2008). "Enhanced depositional and AVO models for lithologically complex sandstones in the Santos Basin, offshore Brazil". *Petroleum Geoscience 14*(3), pp. 235-243.

Li, C., E. M. Ripley, A. J. Naldrett, A. K. Schmitt, and C. H. Moore. (2009). "Magmatic anhydrite-sulfide assemblages in the plumbing system of the Siberian Traps". *Geology 37*(3), pp. 259-262.

Magee, C., F. Briggs, and C. A.-L. Jackson. (2013a). "Lithological controls on igneous intrusion-induced ground deformation". *Journal of the Geological Society 170*(6), pp. 853-856. DOI: 10.1144/jgs2013-029

Magee, C., O. B. Duffy, K. Purnell, R. E. Bell, C. A. L. Jackson, and M. T. Reeve. (2016a). "Fault-controlled fluid flow inferred from hydrothermal vents imaged in 3D seismic reflection data, offshore NW Australia". *Basin Research 28*(3), pp. 299-318.

Magee, C., E. Hunt-Stewart, and C. A. L. Jackson. (2013b). "Volcano growth mechanisms and the role of sub-volcanic intrusions: Insights from 2D seismic reflection data". *Earth and Planetary Science Letters 373*(0), pp. 41-53.

Magee, C., and C.-L. Jackson. (2020). "Seismic reflection data reveal the 3D structure of the newly discovered Exmouth Dyke Swarm, offshore NW Australia". *Solid Earth 11*(2), pp. 576-606.

Magee, C., C. L. Jackson, and N. Schofield. (2014). "Diachronous sub-volcanic intrusion along deep-water margins: insights from the Irish Rockall Basin". *Basin Research 26*(1), pp. 85-105.

Magee, C., S. M. Maharaj, T. Wrona, and C. A.-L. Jackson. (2015). "Controls on the expression of igneous intrusions in seismic reflection data". *Geosphere 11*(4), pp. 1024-1041.

Magee, C., J. Muirhead, N. Schofield, R. J. Walker, O. Galland, S. Holford, . . . W. McCarthy. (2019). "Structural signatures of igneous sheet intrusion propagation". *Journal of Structural Geology 125*, pp. 148-154.

Magee, C., J. D. Muirhead, A. Karvelas, S. P. Holford, C. A. Jackson, I. D. Bastow, . . . W. McCarthy. (2016b). "Lateral magma flow in mafic sill complexes". *Geosphere 12*(3), pp. 809-841.

Malehmir, A., B. Bergman, B. Andersson, R. Sturk, and M. Johansson. (2018). "Seismic imaging of dyke swarms within the Sorgenfrei–Tornquist Zone (Sweden) and implications for thermal energy storage". *Solid Earth 9*(6), pp. 1469-1485.

Mark, N., N. Schofield, D. Gardiner, L. Holt, C. Grove, D. Watson, . . . H. Poore. (2019). "Overthickening of sedimentary sequences by igneous intrusions". *Journal of the Geological Society 176*(1), pp. 46-60.

Meisling, K. E., P. R. Cobbold, and V. S. Mount. (2001). "Segmentation of an obliquely rifted margin, Campos and Santos basins, southeastern Brazil". *AAPG Bulletin 85*(11), pp. 1903-1924.

Menand, T. (2011). "Physical controls and depth of emplacement of igneous bodies: A review". *Tectonophysics 500*(1), pp. 11-19.

Modica, C. J., and E. R. Brush. (2004). "Postrift sequence stratigraphy, paleogeography, and fill history of the deep-water Santos Basin, offshore southeast Brazil". *AAPG Bulletin 88*(7), pp. 923-945.

Mohriak, W. (2003). *Bacias sedimentares da margem continental Brasileira* (Vol. 3): CPRM Brasília.

Mohriak, W., J. Macedo, R. Castellani, H. Rangel, A. Barros, M. Latgé, . . . J. Rizzo. (1995). Salt tectonics and structural styles in the deep-water province of the Cabo Frio region, Rio de Janeiro, Brazil. In M. Jackson, D. Roberts, and S. Snelson (Eds.), *Salt tectonics: a global* *perspective* (Vol. 65, pp. 273-304). AAPG Memoir: American Association of Petroleum Geologists.

Mohriak, W., M. Nóbrega, M. Odegard, B. Gomes, and W. Dickson. (2010). "Geological and geophysical interpretation of the Rio Grande Rise, south-eastern Brazilian margin: extensional tectonics and rifting of continental and oceanic crusts". *Petroleum Geoscience 16*, pp. 231-245.

Mohriak, W., P. Szatmari, and S. M. C. Anjos. (2009). "Sal: Geologia e Tectônica; Exemplos nas Bacias Brasileiras". *Terrae Didatica 4*(1), pp. 90-91.

Oreiro, S. G., J. A. Cupertino, P. Szatmari, and A. T. Filho. (2008). "Influence of pre-salt alignments in post-Aptian magmatism in the Cabo Frio High and its surroundings, Santos and Campos basins, SE Brazil: An example of non-plume-related magmatism". *Journal of South American Earth Sciences 25*(1), pp. 116-131.

Pang, K.-N., N. Arndt, H. Svensen, S. Planke, A. Polozov, S. Polteau, . . . S.-L. Chung. (2013). "A petrologic, geochemical and Sr–Nd isotopic study on contact metamorphism and degassing of Devonian evaporites in the Norilsk aureoles, Siberia". *Contributions to Mineralogy and Petrology 165*(4), pp. 683-704.

Peel, F. J. (2014). "The engines of gravity-driven movement on passive margins: Quantifying the relative contribution of spreading vs. gravity sliding mechanisms". *Tectonophysics 633*, pp. 126-142.

Pequeno, M. A. (2009). *Albian/Maastrichtian tectono-stratigraphic evolution of central Santos Basin, offshore Brazil.* (Masters), University of Texas at Austin, Austin.

Peron-Pinvidic, G., G. Manatschal, and a. t. I. R. W. Participants. (2019). "Rifted margins: state of the art and future challenges". *Frontiers in Earth Science 7*, pp. 8.

Pichel, L., E. Finch, and R. Gawthorpe. (2019a). "The Impact of Pre-Salt Rift Topography on Salt Tectonics: A Discrete-Element Modeling Approach". *Tectonics 38*(4), pp. 1466-1488.

Pichel, L., and C.-L. Jackson. (2020). "Four-dimensional Variability of Composite Halokinetic Sequences". *Basin Research*. DOI: 10.1111/bre.12428

Pichel, L. M., C. A. L. Jackson, F. Peel, and T. P. Dooley. (2019b). "Base-salt relief controls salt-tectonic structural style, São Paulo Plateau, Santos Basin, Brazil". *Basin Research 32*, pp. 453-484.

Pichel, L. M., F. Peel, C. A. Jackson, and M. J. J. o. S. G. Huuse. (2018). "Geometry and kinematics of salt-detached ramp syncline basins". *115*, pp. 208-230.

Planke, S., T. Rasmussen, S. S. Rey, and R. Myklebust. (2005). Seismic characteristics and distribution of volcanic intrusions and hydrothermal vent complexes in the Vøring and Møre basins. In A. G. Doré (Ed.), *Petroleum Geology: North-West Europe and Global Perspectives - Proceddings of the 6th Petroleum Geology Conference* (pp. 833-844): Geological Society, London.

Pollard, D. D., and A. M. Johnson. (1973). "Mechanics of growth of some laccolithic intrusions in the Henry Mountains, Utah, II: bending and failure of overburden layers and sill formation". *Tectonophysics 18*(3), pp. 311-354.

Pollard, D. D., O. H. Muller, and D. R. Dockstader. (1975). "The form and growth of fingered sheet intrusions". *Geological Society of America Bulletin 86*(3), pp. 351-363.

Quirk, D. G., N. Schødt, B. Lassen, S. J. Ings, D. Hsu, K. K. Hirsch, and C. Von Nicolai. (2012). Salt tectonics on passive margins: examples from Santos, Campos and Kwanza basins. In G. Alsop, S. Archer, A. Hartley, G. NT, and R. Hodgkinson (Eds.), *Salt deposition, loading* *and gravity drainage in the Campos and Santos salt basins* (Vol. 363, pp. 207-244). London: Geological Society, London, Special Publications.

Reeves, J., C. Magee, and C. A. L. Jackson. (2018). "Unravelling intrusion-induced forced fold kinematics and ground deformation using 3D seismic reflection data". *Volcanica 1*(1), pp. 1-17.

Reynolds, P., N. Schofield, R. J. Brown, and S. P. Holford. (2018). "The architecture of submarine monogenetic volcanoes–insights from 3D seismic data". *Basin Research 30*, pp. 437-451.

Ripley, E. M., P. C. Lightfoot, C. Li, and E. R. Elswick. (2003). "Sulfur isotopic studies of continental flood basalts in the Noril'sk region: Implications for the association between lavas and ore-bearing intrusions". *Geochimica et Cosmochimica Acta 67*(15), pp. 2805-2817.

Rodriguez, C., C.-L. Jackson, A. Rotevatn, R. Bell, and M. Francis. (2018). "Dual tectonic-climatic controls on salt giant deposition in the Santos Basin, offshore Brazil". *Geosphere 14*(1), pp. 215-242.

Rohrman, M. (2007). "Prospectivity of volcanic basins: Trap delineation and acreage de-risking". *AAPG Bulletin 91*(6), pp. 915-939.

Rowan, M. (2014). "Passive-margin salt basins: hyperextension, evaporite deposition, and salt tectonics". *Basin Research 26*(1), pp. 154-182.

Rowan, M. G., F. J. Peel, and B. C. Vendeville. (2004). *Gravity-driven fold belts on passive margins* (Vol. 82). AAPG Memoir: American Association of Petroleum Geologists.

Schmiedel, T., O. Galland, and C. Breitkreuz. (2017). "Dynamics of sill and laccolith emplacement in the brittle crust: Role of host rock strength and deformation mode". *Journal of Geophysical Research: Solid Earth 122*(11), pp. 8860-8871.

Schmiedel, T., O. Galland, Ø. Haug, G. Dumazer, and C. Breitkreuz. (2019). "Coulomb failure of Earth's brittle crust controls growth, emplacement and shapes of igneous sills, saucer-shaped sills and laccoliths". *Earth and Planetary Science Letters 510*, pp. 161-172.

Schofield, N., I. Alsop, J. Warren, J. R. Underhill, R. Lehné, W. Beer, and V. Lukas. (2014). "Mobilizing salt: Magma-salt interactions". *Geology 42*(7), pp. 599-602.

Schofield, N., S. Holford, J. Millett, D. Brown, D. Jolley, S. R. Passey, . . . C. Stevenson. (2017). "Regional magma plumbing and emplacement mechanisms of the Faroe-Shetland Sill Complex: implications for magma transport and petroleum systems within sedimentary basins". *Basin Research 29*(1), pp. 41-63.

Schofield, N., C. Stevenson, and T. Reston. (2010). "Magma fingers and host rock fluidization in the emplacement of sills". *Geology 38*(1), pp. 63-66.

Schofield, N. J., D. J. Brown, C. Magee, and C. T. Stevenson. (2012). "Sill morphology and comparison of brittle and non-brittle emplacement mechanisms". *Journal of the Geological Society 169*(2), pp. 127-141.

Skogseid, J., S. Planke, J. I. Faleide, T. Pedersen, O. Eldholm, and F. Neverdal. (2000). NE Atlantic continental rifting and volcanic margin formation. In A. Nottvedt (Ed.), *Dynamics of the Norwegian Margin* (Vol. 167, pp. 295-326). London: Geological Society, London, Special Publications.

Spacapan, J. B., O. Galland, H. A. Leanza, and S. Planke. (2017). "Igneous sill and finger emplacement mechanism in shale-dominated formations: a field study at Cuesta del Chihuido, Neuquén Basin, Argentina". *Journal of the Geological Society 174*(3), pp. 422-433.

Stearns, D. W. (1978). "Faulting and forced folding in the Rocky Mountains foreland". *Geological Society of America Memoirs 151*, pp. 1-38.

Svensen, H., S. Planke, B. Jamtveit, and T. Pedersen. (2003). "Seep carbonate formation controlled by hydrothermal vent complexes: a case study from the Vøring Basin, the Norwegian Sea". *Geo-Marine Letters 23*(3-4), pp. 351-358.

Tari, G., J. Molnar, and P. Ashton. (2003). Examples of salt tectonics from West Africa: a comparative approach. In T. Arthur, D. MacGregor, and N. Cameron (Eds.), *Petroleum Geology of Africa: New Themes and Developing Technologies* (Vol. 207, pp. 85-104). London: Geological Society, London, Special Publications.

Thorsen, C. E. (1963). "Age of growth faulting in southeast Louisiana". *Gulf Coast Association of Geological Societies Transactions 13*, pp. 103-110.

Trude, J., J. Cartwright, R. J. Davies, and J. R. Smallwood. (2003). "New technique for dating igneous sills". *Geology 31*, pp. 4.

Underhill, J. R. (2009). "Role of intrusion-induced salt mobility in controlling the formation of the enigmatic ‘Silverpit Crater’, UK Southern North Sea". *Petroleum Geoscience 15*(3), pp. 197-216.

Urai, J. L., C. J. Spiers, H. J. Zwart, and G. S. Lister. (1986). "Weakening of rock salt by water during long-term creep". *Nature 324*(6097), pp. 554-557.

Van Keken, P., C. Spiers, A. Van den Berg, and E. Muyzert. (1993). "The effective viscosity of rocksalt: implementation of steady-state creep laws in numerical models of salt diapirism". *Tectonophysics 225*(4), pp. 457-476.

Vendeville, B. C., and M. P. Jackson. (1992). "The rise of diapirs during thin-skinned extension". *Marine and petroleum geology 9*(4), pp. 331-354.

934 Walker, R. J. (2016). "Controls on transgressive sill growth". *Geology 44*(2), pp. 99-102.

935 Warren, J. K. (2006). *Evaporites: sediments, resources and hydrocarbons*. Berlin: Springer Science & Business Media.

937 Warren, J. K. (2010). "Evaporites through time: Tectonic, climatic and eustatic controls in marine and nonmarine deposits". *Earth-Science Reviews 98*(3-4), pp. 217-268.

Highlights

1) Magma inevitably intrudes salt in some basins, but what are the consequences of such interaction?

2) Use seismic reflection images of sills below, within, and above salt in the Santos Basin, Brazil

3) We show the salt trapped ascending magma in places, whereas other areas were bypassed by dykes

4) Intrusion of hot magma enhanced salt flow, but crystallised sills inhibited later salt movement

5) Salt rheology and structure impacts magma plumbing systems, which in turn impacts salt tectonics

Figure 1

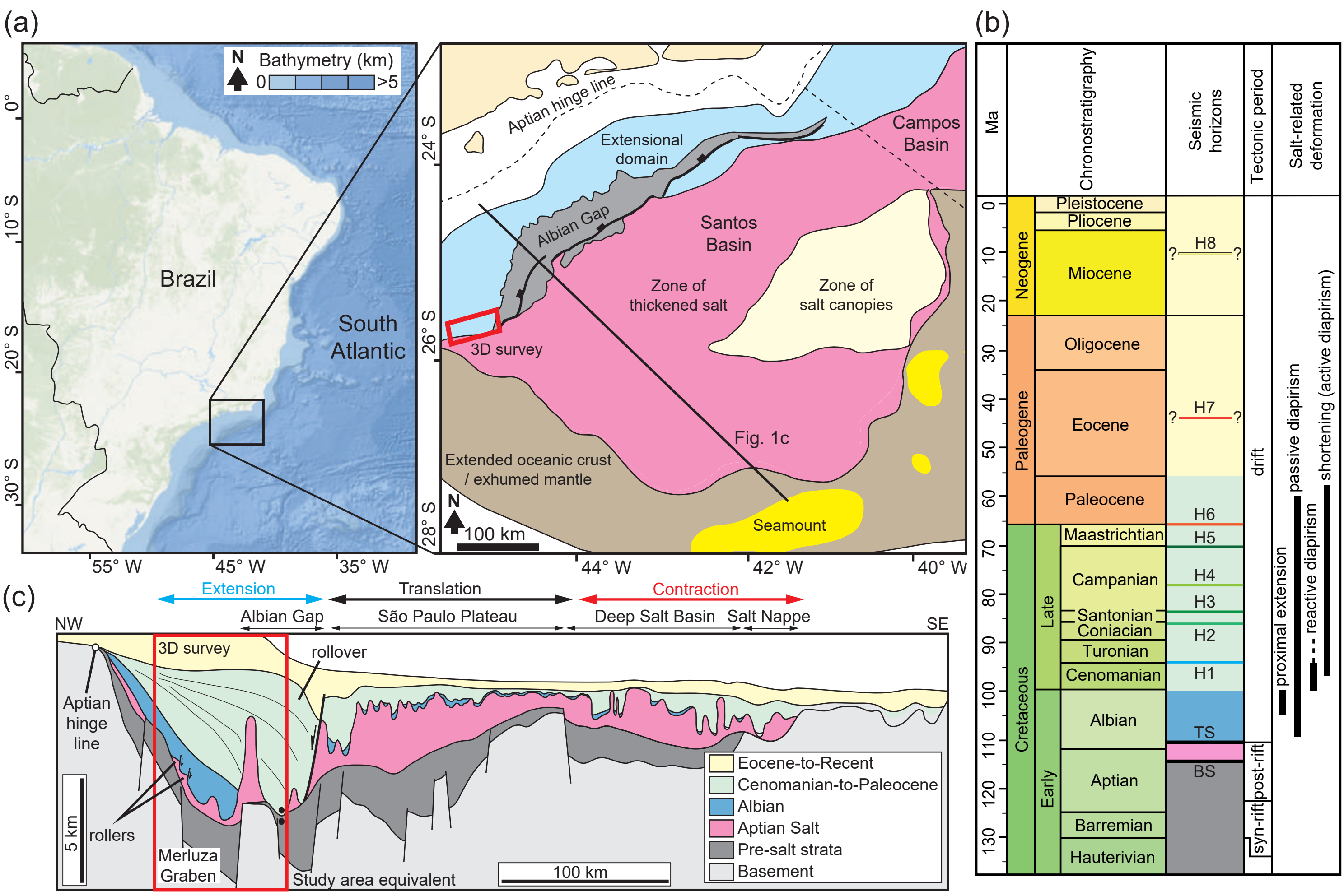
(a)
Bathymetry (km)
0
>5
N
Brazil
South Atlantic
0°
10° S
20° S
30° S
55° W
45° W
35° W
Aptian hinge line
Extensional domain
Campos Basin
Albian Gap
Santos Basin
Zone of thickened salt
Zone of salt canopies
3D survey
Fig. 1c
Extended oceanic crust / exhumed mantle
Seamount
100 km
24° S
26° S
28° S
44° W
42° W
40° W
(b)
Ma
Chronostratigraphy
Seismic horizons
Tectonic period
Salt-related deformation
Neogene
Paleogene
Cretaceous
Late
Early
Pleistocene
Pliocene
Miocene
Oligocene
Eocene
Paleocene
Maastrichtian
Campanian
Santonian
Coniacian
Turonian
Cenomanian
Albian
Aptian
Barremian
Hauterivian
H8
H7
H6
H5
H4
H3
H2
H1
TS
BS
drift
post-rift
syn-rift
proximal extension
passive diapirism
reactive diapirism
shortening (active diapirism)
(c)
Extension
Translation
Contraction
NW
SE
Albian Gap
São Paulo Plateau
Deep Salt Basin
Salt Nappe
3D survey
rollover
Aptian hinge line
rollers
Merluza Graben
Study area equivalent
5 km
100 km
Eocene-to-Recent
Cenomanian-to-Paleocene
Albian
Aptian Salt
Pre-salt strata
Basement

Figure 2

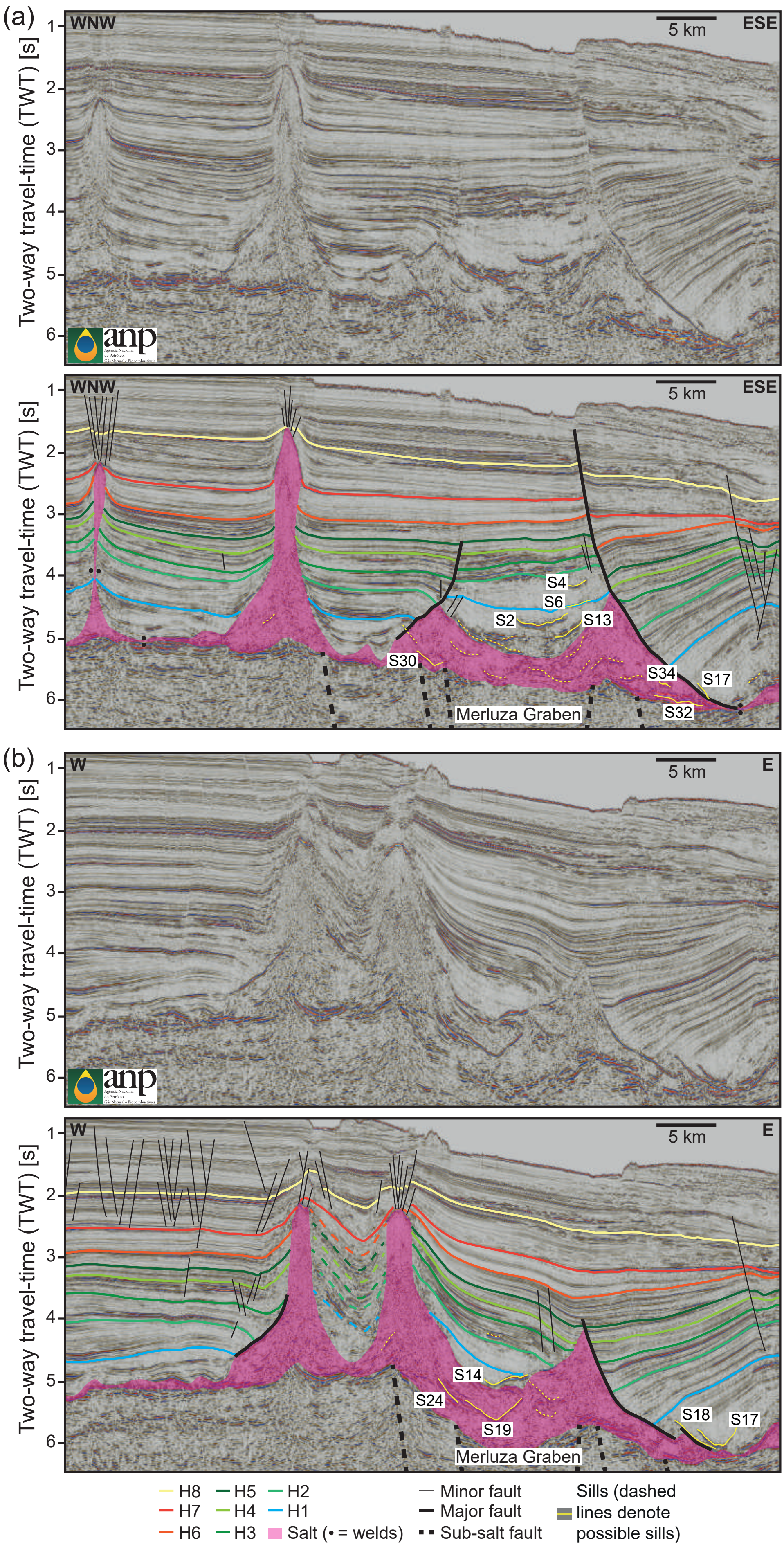
(a)
WNW
ESE
5 km
Two-way travel-time (TWT) [s]
anp
S4
S6
S2
S13
S30
S34
S17
S32
Merluza Graben
(b)
W
E
S14
S24
S19
S18
Merluza Graben
H8
H7
H6
H5
H4
H3
H2
H1
Salt (• = welds)
Minor fault
Major fault
Sub-salt fault
Sills (dashed lines denote possible sills)

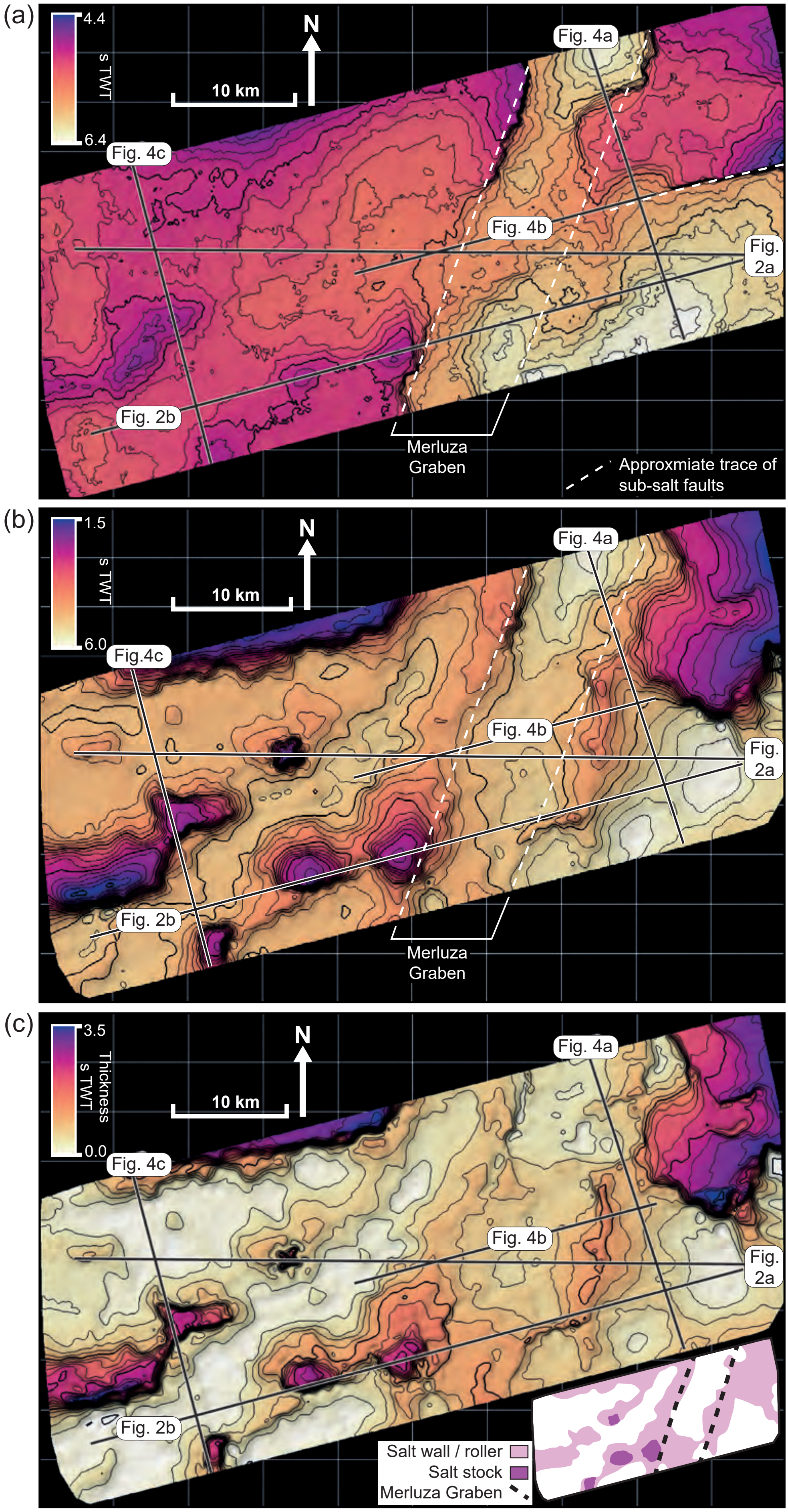
(a)
4.4
s TWT
6.4
N
10 km
Fig. 4a
Fig. 4c
Fig. 4b
Fig. 2a
Fig. 2b
Merluza Graben
Approxmiate trace of sub-salt faults
(b)
1.5
s TWT
6.0
N
10 km
Fig. 4a
Fig.4c
Fig. 4b
Fig. 2a
Fig. 2b
Merluza Graben
(c)
3.5
Thickness s TWT
0.0
N
10 km
Fig. 4a
Fig. 4c
Fig. 4b
Fig. 2a
Fig. 2b
Salt wall / roller
Salt stock
Merluza Graben

Figure 4

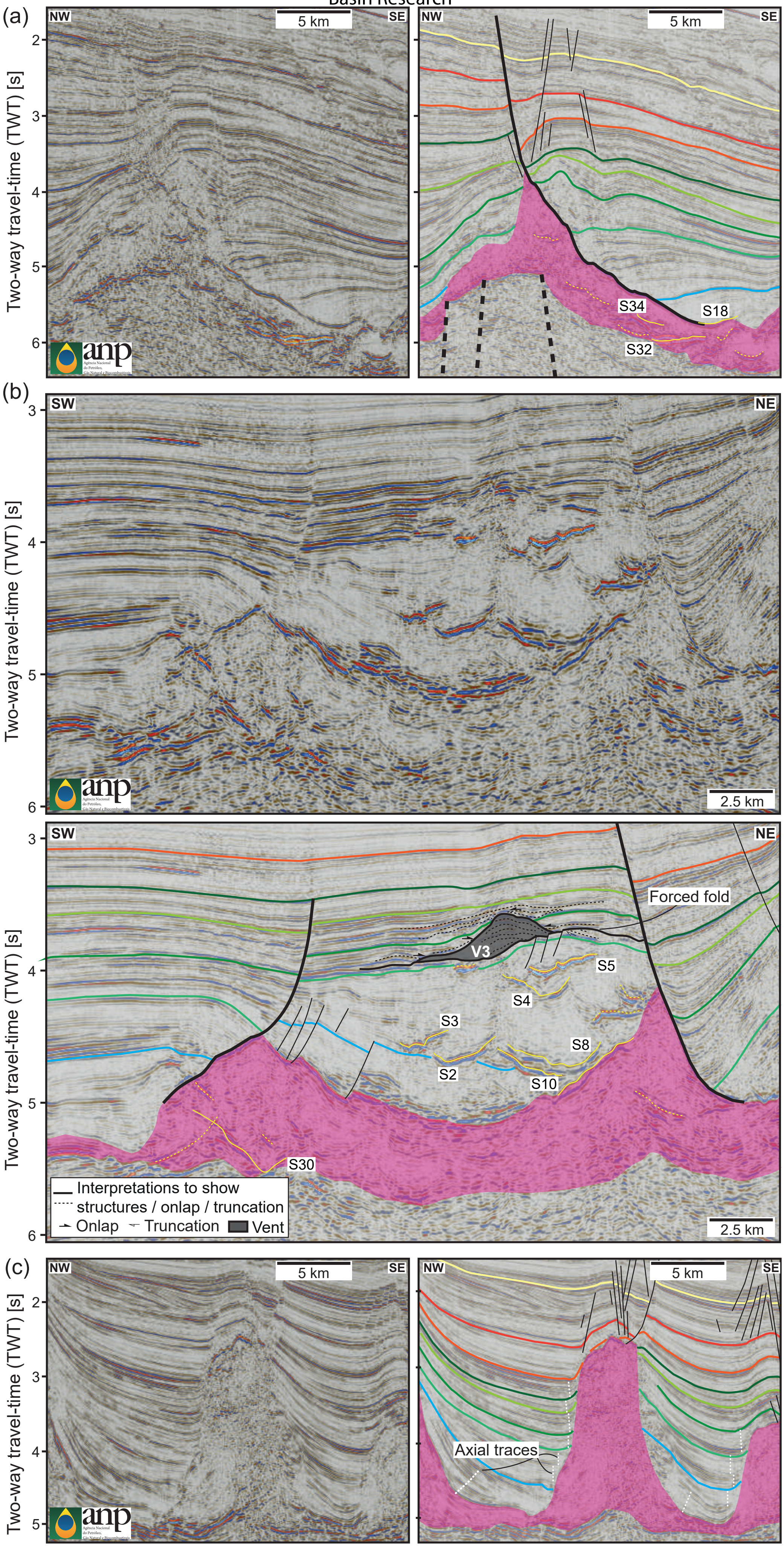

(a)
NW
5 km
SE
NW
5 km
SE
Two-way travel-time (TWT) [s]
2
3
4
5
6
anp
S34
S18
S32
(b)
SW
NE
3
4
5
6
2.5 km
Forced fold
V3
S5
S4
S3
S8
S2
S10
S30
Interpretations to show
structures / onlap / truncation
Onlap
Truncation
Vent
(c)
Axial traces

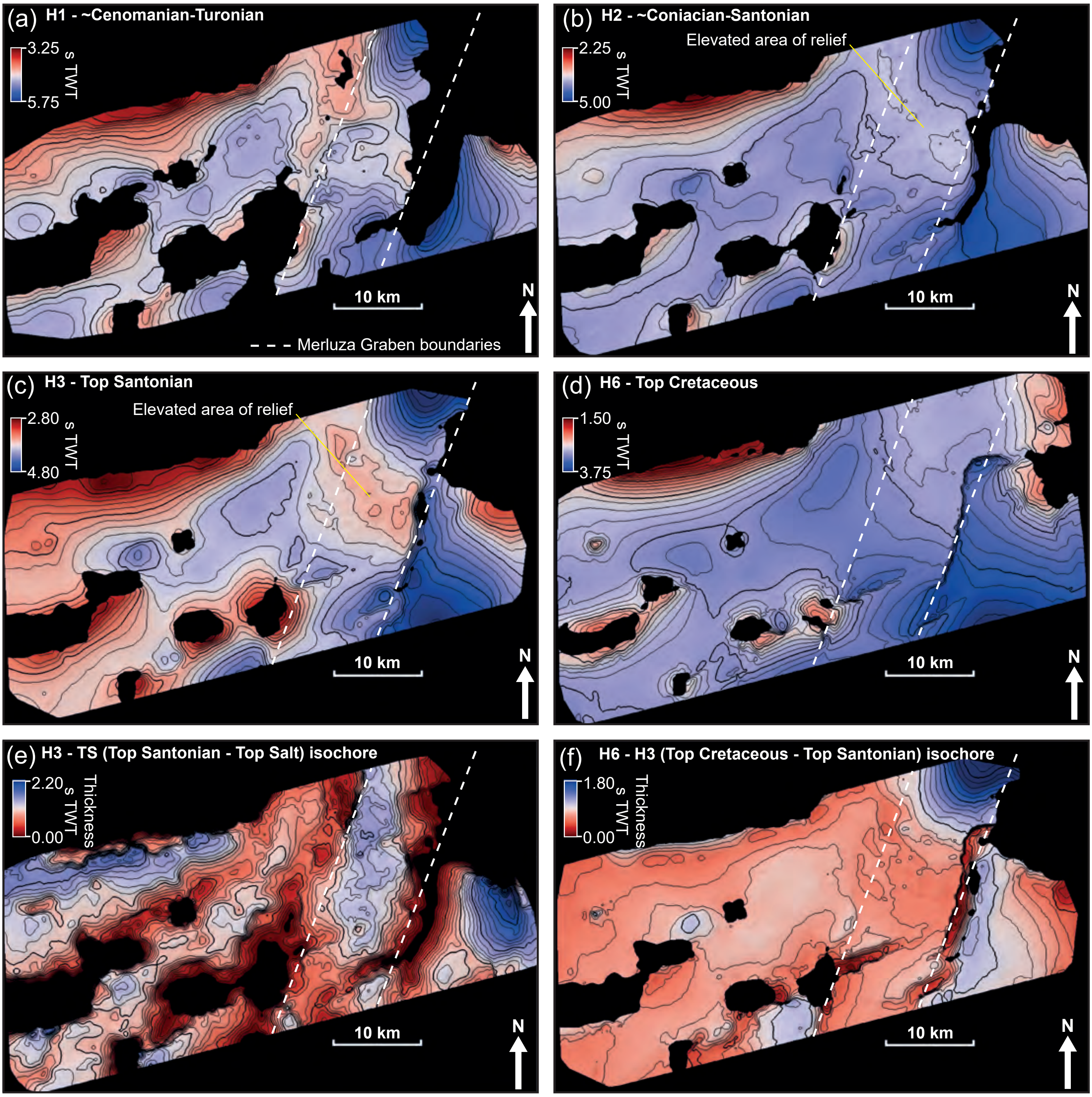
(a) H1 - ~Cenomanian-Turonian
3.25
5.75
s TWT
10 km
N
- - - Merluza Graben boundaries
(b) H2 - ~Coniacian-Santonian
Elevated area of relief
2.25
5.00
s TWT
10 km
N
(c) H3 - Top Santonian
Elevated area of relief
2.80
4.80
s TWT
10 km
N
(d) H6 - Top Cretaceous
1.50
3.75
s TWT
10 km
N
(e) H3 - TS (Top Santonian - Top Salt) isochore
2.20
0.00
s TWT
Thickness
10 km
N
(f) H6 - H3 (Top Cretaceous - Top Santonian) isochore
1.80
0.00
s TWT
Thickness
10 km
N

Figure 6

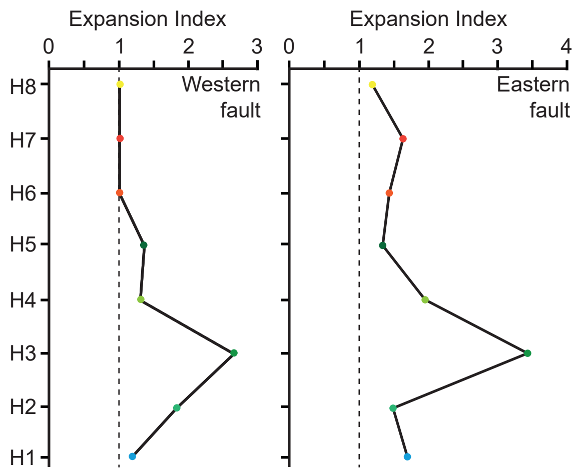
Expansion Index
0
1
2
3
Western
fault
H8
H7
H6
H5
H4
H3
H2
H1
Expansion Index
0
1
2
3
4
Eastern
fault

Figure 7

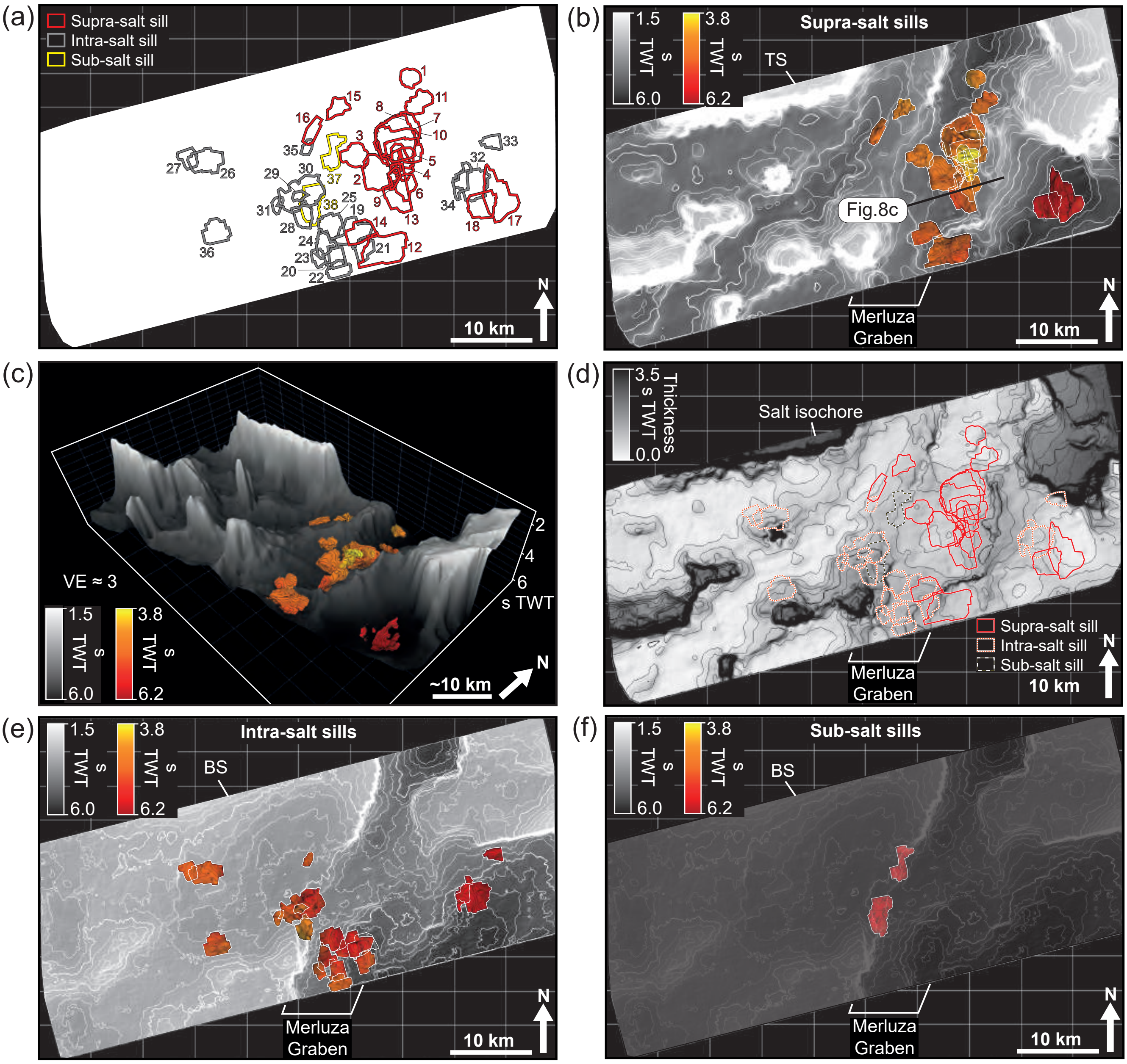
(a)
Supra-salt sill
Intra-salt sill
Sub-salt sill
10 km
N
(b)
Supra-salt sills
1.5
6.0
TWT s
3.8
6.2
TWT s
TS
Fig.8c
Merluza Graben
10 km
N
(c)
VE ≈ 3
1.5
6.0
TWT s
3.8
6.2
TWT s
2
4
6
s TWT
~10 km
N
(d)
3.5
0.0
Thickness s TWT
Salt isochore
Supra-salt sill
Intra-salt sill
Sub-salt sill
Merluza Graben
10 km
N
(e)
1.5
6.0
TWT s
3.8
6.2
TWT s
Intra-salt sills
BS
Merluza Graben
10 km
N
(f)
1.5
6.0
TWT s
3.8
6.2
TWT s
Sub-salt sills
BS
Merluza Graben
10 km
N

Figure 8

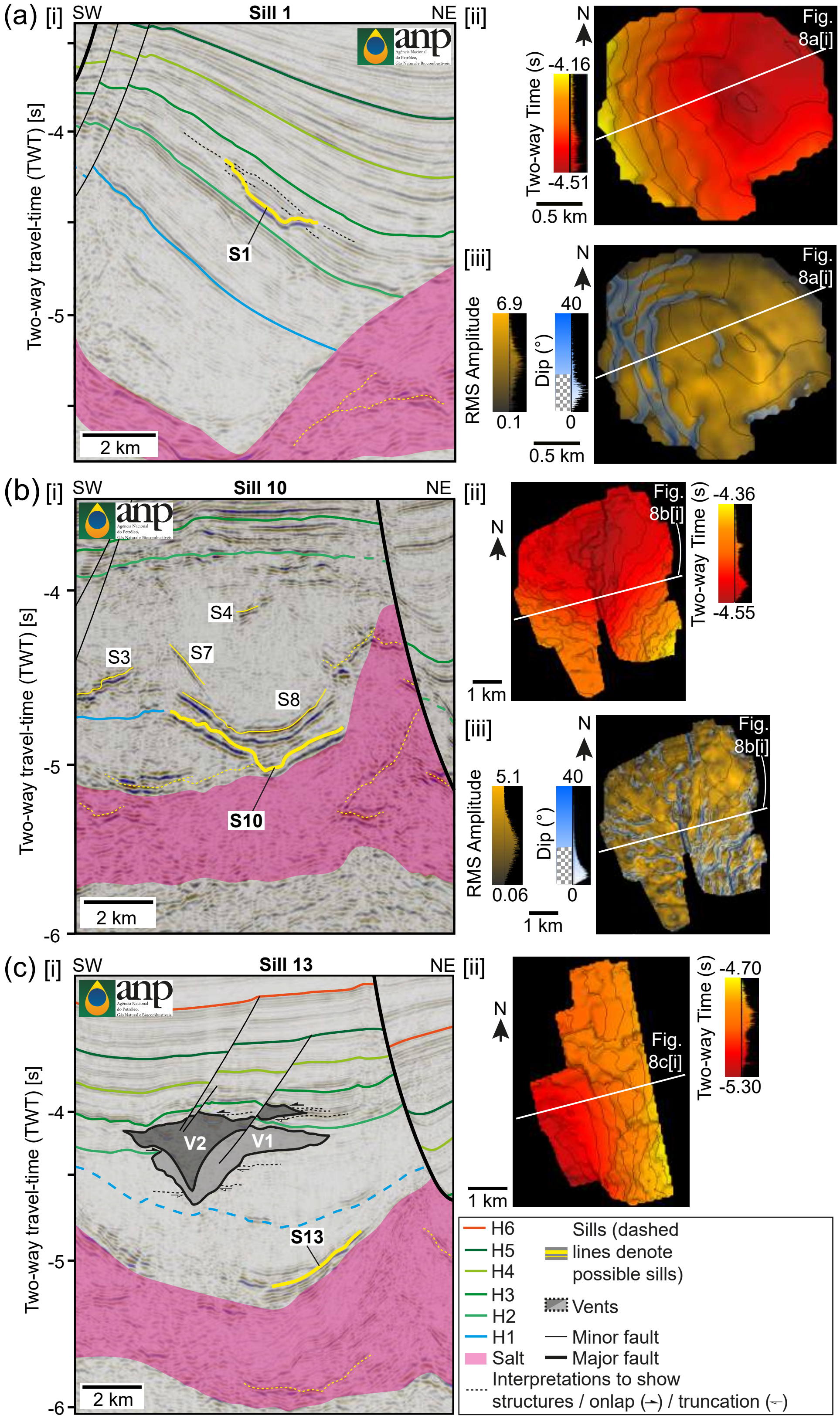
(a) [i] SW
Sill 1
NE [ii]
Two-way travel-time (TWT) [s]
-4
-5
S1
2 km
N
Two-way Time (s)
-4.16
-4.51
0.5 km
Fig. 8a[i]
[iii]
RMS Amplitude
6.9
0.1
Dip (°)
40
0
0.5 km
Fig. 8a[i]
(b) [i] SW
Sill 10
NE [ii]
-4
-5
-6
S4
S3
S7
S8
S10
2 km
Fig. 8b[i]
Two-way Time (s)
-4.36
-4.55
1 km
[iii]
RMS Amplitude
5.1
0.06
Dip (°)
40
0
1 km
Fig. 8b[i]
(c) [i] SW
Sill 13
NE [ii]
-4
-5
-6
V2
V1
S13
2 km
N
Fig. 8c[i]
Two-way Time (s)
-4.70
-5.30
1 km
H6
H5
H4
H3
H2
H1
Salt
Sills (dashed lines denote possible sills)
Vents
Minor fault
Major fault
Interpretations to show structures / onlap (⌐) / truncation (⌐)

Figure 9

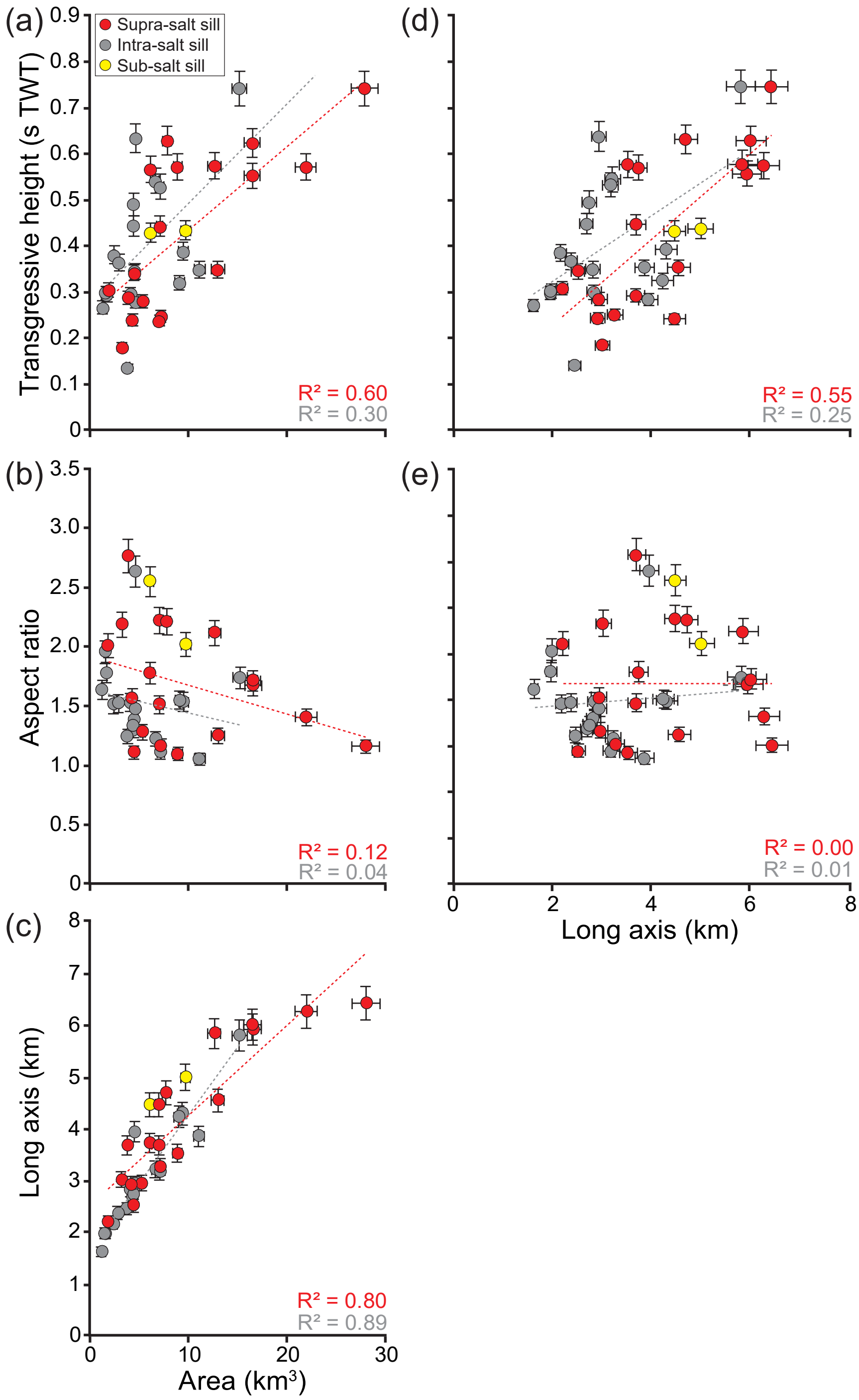
(a)
Supra-salt sill
Intra-salt sill
Sub-salt sill
Transgressive height (s TWT)
R² = 0.60
R² = 0.30
(b)
Aspect ratio
R² = 0.12
R² = 0.04
(c)
Long axis (km)
R² = 0.80
R² = 0.89
Area (km³)
(d)
R² = 0.55
R² = 0.25
(e)
R² = 0.00
R² = 0.01
Long axis (km)

Figure 10

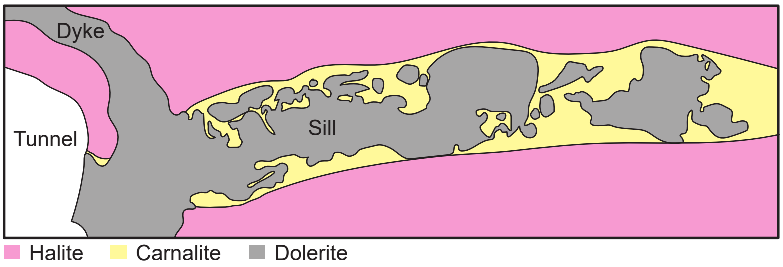

Figure 11

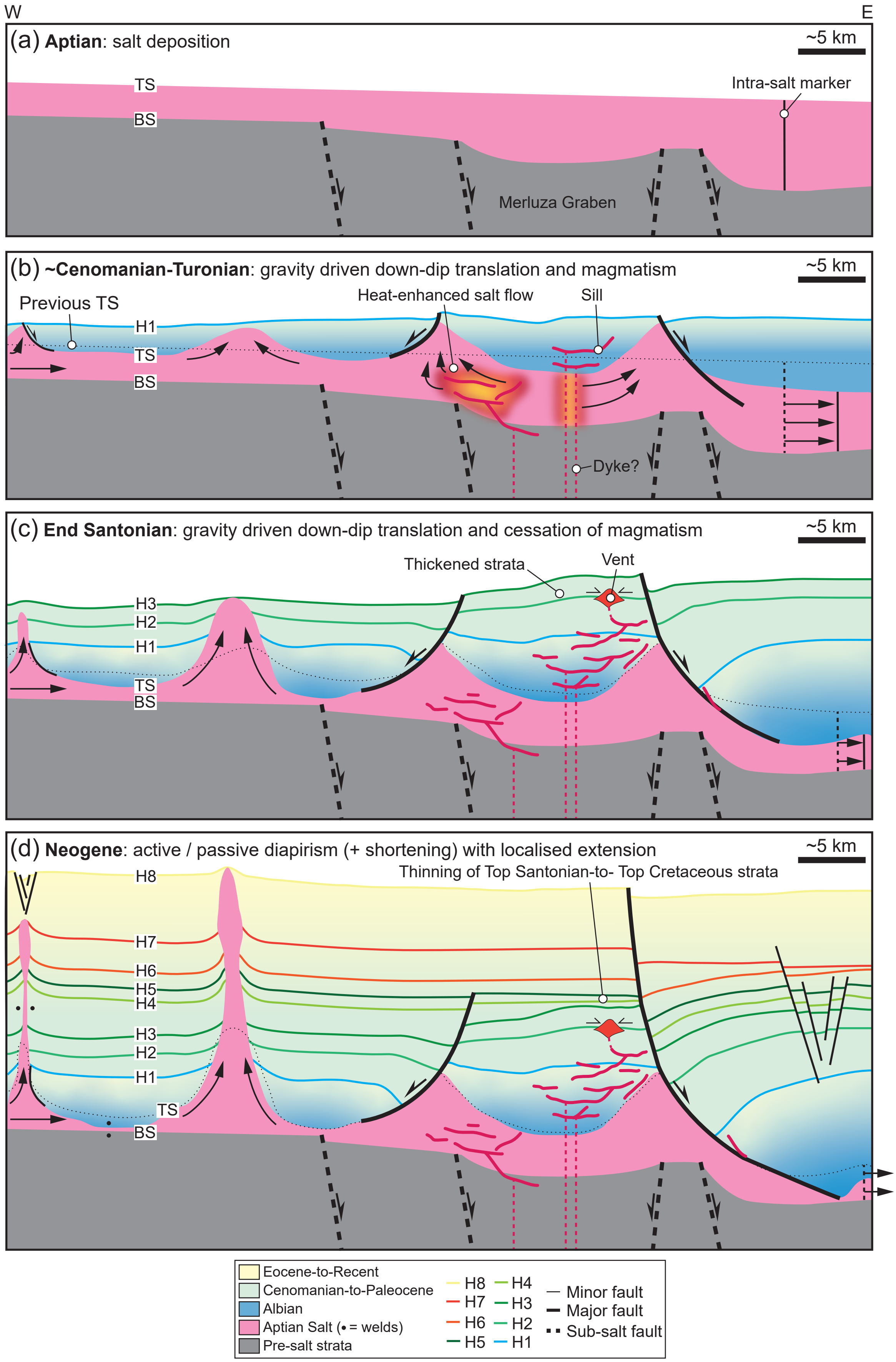
W
E
(a) Aptian: salt deposition
~5 km
TS
BS
Intra-salt marker
Merluza Graben
(b) ~Cenomanian-Turonian: gravity driven down-dip translation and magmatism
~5 km
Previous TS
Heat-enhanced salt flow
Sill
H1
TS
BS
Dyke?
(c) End Santonian: gravity driven down-dip translation and cessation of magmatism
~5 km
Thickened strata
Vent
H3
H2
H1
TS
BS
(d) Neogene: active / passive diapirism (+ shortening) with localised extension
~5 km
Thinning of Top Santonian-to- Top Cretaceous strata
H8
H7
H6
H5
H4
H3
H2
H1
TS
BS
Eocene-to-Recent
Cenomanian-to-Paleocene
Albian
Aptian Salt (• = welds)
Pre-salt strata
H8
H7
H6
H5
H4
H3
H2
H1
Minor fault
Major fault
Sub-salt fault

Table 1: Sill measurements and position information

Sill number	Style	Area (km^2)	Major axis (km)	Minor axis (km)	Aspect ratio	Maximum depth (ms TWT)	Minimum depth (ms TWT)	Height (ms TWT)	Position relative to salt	Top sill termination depth
1	Saucer	04.5	2.53	2.27	1.11	4505.6	4163.6	341.9	Above	Above Coniacian-Santonian
2	Saucer	13.0	4.55	3.63	1.25	4872.5	4523.4	349.1	Above	Above Turonian
3	Saucer	07.2	3.27	2.80	1.17	4695.2	4447.9	247.3	Above	Above Turonian
4	Saucer	07.0	4.47	2.00	2.23	4226.3	3988.0	238.3	Above	Above Turonian
5	Saucer	03.3	3.02	1.38	2.19	4021.3	3840.6	180.7	Above	Above Turonian
6	Saucer	05.3	2.96	2.30	1.29	4650.6	4369.6	281.0	Above	Above Turonian
7	Saucer	07.8	4.70	2.12	2.22	4835.4	4207.1	628.3	Above	Above Turonian (probably)
8	Saucer	21.9	6.27	4.44	1.41	5015.5	4444.5	571.0	Above	Above Turonian (probably)
9	Saucer	01.9	2.22	1.10	2.02	4785.1	4480.5	304.6	Above	Above Turonian (probably)
10	Saucer	27.9	6.42	5.52	1.16	5105.4	4363.6	741.8	Above	Above Turonian (probably)
11	Inclined	06.1	3.74	2.09	1.78	5046.1	4479.5	566.6	Above	Above Turonian (probably)
12	Strata-concordant	16.5	5.93	3.54	1.68	5174.1	4621.0	553.1	Above	Above Turonian (probably)
13	Strata-concordant	12.6	5.84	2.75	2.12	5281.8	4707.3	574.5	Above	Above Turonian (probably)
14	Transgressive	07.1	3.69	2.43	1.52	5153.0	4709.9	443.2	Above	Above Turonian
15	Transgressive	04.3	2.93	1.87	1.57	4539.5	4299.7	239.9	Above	Above Turonian
16	Transgressive	03.9	3.69	1.33	2.77	4814.5	4525.8	288.8	Above	Above Turonian (probably)
17	Saucer	16.5	6.01	3.49	1.72	6114.5	5490.2	624.3	Above	Above salt
18	Transgressive	08.9	3.53	3.21	1.10	6168.3	5596.0	572.3	Above	Above salt
19	Saucer	09.4	4.30	2.79	1.54	5658.3	5269.9	388.5	Within	Below top salt
20	Inclined	04.4	2.70	2.07	1.30	5378.7	4934.9	443.8	Within	Below top salt
21	Saucer	04.5	2.83	2.03	1.39	5348.2	5003.0	345.2	Within/above	Above salt
22	Transgressive	04.1	2.84	1.85	1.53	5028.0	4732.0	296.0	Within/above	Above salt
23	Inclined	02.5	2.18	1.43	1.52	5133.7	4752.5	381.2	Within	Below top salt
24	Inclined	04.4	2.75	2.06	1.34	5468.2	4977.4	490.8	Within	Below top salt
25	Inclined	06.7	3.22	2.63	1.23	5649.1	5107.2	541.9	Within	Below top salt
26	Sub-horizontal	09.1	4.24	2.73	1.55	5218.8	4898.2	320.6	Within	Below top salt
27	Sub-horizontal	03.8	2.47	1.98	1.25	5103.1	4966.6	136.5	Within	Below top salt
28	Inclined	04.6	2.95	2.00	1.47	4658.5	4024.9	633.7	Within	Below top salt
29	Inclined	01.3	1.64	1.00	1.64	4759.0	4492.1	266.9	Within	Below top salt
30	Saucer	15.2	5.80	3.33	1.74	5527.5	4785.2	742.3	Within	Below top salt
31	Inclined	01.7	1.98	1.11	1.79	4957.9	4663.5	294.4	Within	Below top salt
32	Saucer	11.1	3.86	3.65	1.06	6194.3	5844.9	349.4	Within	Below top salt
33	Inclined	02.9	2.38	1.56	1.53	5852.9	5489.0	363.9	Within	Below top salt
34	Saucer	04.6	3.94	1.49	2.64	5877.2	5597.2	280.0	Within	Below top salt
35	Inclined	01.6	1.99	1.01	1.96	5147.2	4848.6	298.6	Within	Below top salt
36	Transgressive	07.1	3.18	2.85	1.12	5256.5	4727.6	529.0	Within	Below top salt
37	Transgressive	06.1	4.47	1.75	2.55	5911.0	5481.9	429.1	Below/within	Below top salt
38	Transgressive	09.7	5.00	2.47	2.02	5930.9	5496.5	434.5	Below/within	Below top salt